

# Simulated Operational Testing of the Prototype Implementation of the SOFIE Model: The 2025 Space Weather Prediction Testbed Exercise

Weihaio Liu<sup>1</sup>, Lulu Zhao<sup>1</sup>, Igor V. Sokolov<sup>1</sup>, Kathryn Whitman<sup>2,3</sup>,  
Tamas I. Gombosi<sup>1</sup>, Nishtha Sachdeva<sup>1</sup>, Eric T. Adamson<sup>4</sup>, Hazel M.  
Bain<sup>4,5</sup>, Claudio Corti<sup>6,7,8</sup>, M. Leila Mays<sup>6</sup>, Michelangelo Romano<sup>6,9</sup>,  
Carina R. Alden<sup>6,9</sup>, Madeleine M. Anastopoulos<sup>6,9</sup>, Mary E. Aronne<sup>6,10</sup>,  
Janet E. Barzilla<sup>2,11</sup>, Wesley T. Cook<sup>4</sup>, Shawn D. Dahl<sup>4</sup>, Hannah  
Hermann<sup>6,9</sup>, Anthony J. Iampietro<sup>6,9</sup>, A. Steve Johnson<sup>2,11</sup>, Elizabeth A.  
Juelfs<sup>6,10</sup>, Melissa R. Kane<sup>6,9</sup>, Jonathan D. Lash<sup>4</sup>, Kimberly Moreland<sup>4,5</sup>,  
Briana K. Muhlestein<sup>4</sup>, Teresa Nieves-Chinchilla<sup>6</sup>, Edward Semones<sup>2</sup>, James  
F. Spann<sup>12</sup>, Earl M. Spencer<sup>4</sup>, Luke A. Stegeman<sup>2,11</sup>, Christopher J.  
Stubenrauch<sup>6,9</sup>, Kenneth L. Tegnell<sup>4</sup>

<sup>1</sup>Department of Climate and Space Sciences and Engineering, University of Michigan, Ann Arbor, MI  
48109, USA

<sup>2</sup>Space Radiation Analysis Group, NASA Johnson Space Center, Houston, TX 77058, USA

<sup>3</sup>KBR, Houston, TX 77002, USA

<sup>4</sup>NOAA Space Weather Prediction Center, Boulder, CO 80305, USA

<sup>5</sup>Cooperative Institute for Research In Environmental Sciences, University of Colorado, Boulder, CO  
80309, USA

<sup>6</sup>Heliophysics Science Division, NASA Goddard Space Flight Center, Greenbelt, MD 20771, USA

<sup>7</sup>Universities Space Research Association, Washington, DC 20024, USA

<sup>8</sup>Physics and Astronomy Department, University of Hawaii at Manoa, Honolulu, HI 96822, USA

<sup>9</sup>Department of Physics, The Catholic University of America, Washington, DC 20064, USA

<sup>10</sup>Department of Physics and Astronomy, George Mason University, Fairfax, VA 22030, USA

<sup>11</sup>Leidos, Inc., Webster, TX 77598, USA

<sup>12</sup>NOAA NESDIS Office of Space Weather Observations, Silver Spring, MD 20706, USA

---

Corresponding author: Weihaio Liu, [whliu@umich.edu](mailto:whliu@umich.edu)

**Key Points:**

- A prototype of SOFIE, an integrated physics-based model, was run on-site in the 2025 SWPT exercise under simulated operational conditions.
- SOFIE predicts SEP fluxes significantly faster than real time, although the earliest SEP forecast requires a few hours after CME onset.
- Model optimization and forecaster's feedback pave the way for SOFIE's operational utility, supporting future space exploration missions.

**Abstract**

The CLEAR Space Weather Center of Excellence’s solar energetic particle (SEP) model, Solar wind with FIeld lines and Energetic particles (SOFIE), was run and evaluated on-site during the Space Weather Prediction Testbed (SWPT) exercise at the National Oceanic and Atmospheric Administration’s Space Weather Prediction Center (NOAA/SWPC) in May 2025. As a physics-based SEP model, SOFIE simulates the acceleration and transport of energetic particles by the coronal mass ejection (CME)-driven shock in the solar corona and inner heliosphere, and has been validated against historical events. However, questions remain regarding whether a physics-based model, traditionally considered computationally expensive, could meet operational needs. The SWPT exercise offered a valuable opportunity to evaluate SOFIE under simulated operational conditions. On-site interactive feedback from SWPC forecasters, Space Radiation Analysis Group (SRAG) console operators, Community Coordinated Modeling Center (CCMC) personnel, and Moon-to-Mars Space Weather Analysis Office (M2M SWAO) analysts led to significant strategic improvements in the model configuration. The simulation grid was optimized by combining a coarser background grid with higher-resolution regions along the CME path and toward Earth, reducing computational cost without compromising accuracy. In this work, we present the simulated operational performance of SOFIE and its capability to predict SEP fluxes significantly faster than real time. During the SWPT exercise, SOFIE completed a 4-day SEP simulation within 5 hours using 1,000 central processing unit cores, although the earliest SEP forecast was obtained a few hours after CME onset. This marks a milestone in demonstrating SOFIE’s operational usefulness and robustness to support future human space exploration.

**Plain Language Summary**

Solar energetic particles (SEPs) are bursts of high-energy particles released by the Sun, often during large eruptions called coronal mass ejections (CMEs). These particles can reach Earth in less than an hour, posing hazards to satellites, astronauts, and even ground-based technologies. Therefore, reliable SEP predictions are critical for future human space missions. In this work, we describe the operational testing of the Solar wind with FIeld lines and Energetic particles (SOFIE) model during the Space Weather Prediction Testbed (SWPT) exercise at the National Oceanic and Atmospheric Administration’s Space Weather Prediction Center (NOAA/SWPC). SOFIE is an integrated physics-

based model that simulates the solar wind, CME generation and propagation, and shock-driven acceleration and transport processes of SEPs. During the SWPT exercise, SOFIE was run on 1,000 central processing unit cores for two historical events under simulated operational conditions. It reproduced key features of CME coronagraph images and SEP fluxes, delivering 4-day predictions significantly faster than real time, although the earliest SEP forecast was produced a few hours after CME onset. This demonstrates that SOFIE as a physics-based SEP model, although traditionally considered computationally expensive, can provide accurate and real-time SEP predictions, marking an important step toward operational usefulness for future space exploration.

## 1 Motivation

In April and May 2025, the National Oceanic and Atmospheric Administration’s Space Weather Prediction Center (NOAA/SWPC), together with the Community Coordinated Modeling Center (CCMC), the National Aeronautics and Space Administration’s Space Radiation Analysis Group (NASA/SRAG), and the NASA Moon-to-Mars Space Weather Analysis Office (M2M SWAO), hosted the first Space Weather Prediction Testbed (SWPT) exercise (<https://testbed.spaceweather.gov/exercises/2025-artemis-ii-human-spaceflight-support-exercise-information>) in support of the Artemis II mission, marking a major leap forward in operational readiness for human spaceflight. The exercise brought together SWPC forecasters, SRAG console operators, M2M SWAO analysts, CCMC personnel, and experts from commercial industry and academia to evaluate space weather products and operational workflows.

Within this exercise, SWPC, M2M SWAO, CCMC, and SRAG played distinct, but complementary roles. SWPC serves as the official civilian operational forecast center and their forecasters provided the initial solar event alerts, including flare detections. Both SWPC and M2M SWAO characterized the associated coronal mass ejections (CMEs) through the SWPC CME Analysis Tool (SWPC-CAT) and provided these analyses (though the M2M SWAO-derived values were used for our subsequent modeling of the eruptive event). CCMC provides research-to-operations model testing and validation support, and SRAG console operators assess radiation exposure in real time. Specifically, participants worked in small teams through two solar radiation storm scenarios based on the 10 September 2017 and 4 November 2001 solar energetic particle (SEP) events, two strong, well-observed historical events observed at Earth, accompanied by contextual observations of the so-

lar wind, flares, CMEs and SEPs. Radiation levels for both events were simulated inside the Artemis II Orion vehicle: while doses observed inside the vehicle over the course of the simulated events would not pose acute health risks to astronauts, they would exceed the threshold to build shelter, giving SRAG console operators the opportunity to describe the planned space radiation response to Testbed observers. For each event, the exercise examined organizational coordination, technical performance, and strategic decision making, and also tested the accuracy and runtime performance of SEP models for real-time SEP predictions.

The NASA’s Space Weather Center of Excellence, CLEAR, has actively participated in the May 2025 SWPT exercise. During the exercise, the CLEAR team conducted on-site simulations using the SOLar wind with FIeld lines and Energetic particles (SOFIE, Zhao et al., 2024; Liu, Sokolov, et al., 2025) model to test its ability to predict SEP fluxes in real time. In the following, we present the results of SOFIE’s application during the SWPT exercise. In Section 2, we provide a background introduction of SEPs. Section 3 describes the workflow of the SOFIE model. Sections 4 and 5 present the two representative historical SEP events selected for this exercise, the 10 September 2017 and 4 November 2001 eruptions, comparing model results with spacecraft observations. In Section 6, we discuss the operational implications of SOFIE, including lessons learned from the SWPT exercise and the balance between grid resolution and computational efficiency. Finally, Section 7 summarizes the findings and outlines future directions toward operational SEP prediction capabilities.

## 2 Radiation Hazard from SEPs

SEPs are one of the most hazardous manifestations of solar activity for both space- and ground-based systems. Accelerated by shock-driven acceleration and/or magnetic reconnection processes in flares and coronal jets (Desai & Giacalone, 2016; Klein & Dalla, 2017), these high-energy particles are observed to span a wide range of energies from tens of keV to a few GeV, and their spectra evolve dynamically during an event. They can penetrate deep into spacecraft shielding or human tissue, causing short-term increases in radiation levels that can last up to several days (e.g., Mertens & Slaba, 2019; J. Guo et al., 2021; Buzulukova & Tsurutani, 2022; Krittanawong et al., 2022). For human spaceflight beyond Earth’s magnetosphere, SEPs can also threaten satellite electronics, communications, and pose significant radiation risks with radiation levels that can rise rapidly

within minutes to hours (e.g., [Minow et al., 2020](#); [Löwe et al., 2025](#)). Consequently, SEP predictions have long been recognized as a crucial element of space weather operations ([Anastasiadis et al., 2019](#); [Georgoulis et al., 2024](#); [J. Guo et al., 2024](#); [Papaioannou, Strauss, et al., 2025](#)).

In operational practice, NOAA/SWPC radiation storm services are traditionally based on proton intensities in geostationary orbit, as measured by particle detectors on board the Geostationary Operational Environmental Satellites (GOES, [Menzel & Purdom, 1994](#); [Onsager et al., 1996](#); [Rodriguez et al., 2014](#); [Kress et al., 2020](#)). The corresponding SWPC radiation products are based on the NOAA solar radiation storm scale (<https://www.swpc.noaa.gov/noaa-scales-explanation>), which relates the GOES >10 MeV proton flux to impacts on humans, satellite systems, navigation, and other technologies ([Bain et al., 2023](#)). A solar particle event, defined as the >10 MeV proton flux exceeding 10 particle flux units (pfu,  $\# \text{ cm}^{-2} \text{ s}^{-1} \text{ sr}^{-1}$ ), poses a potential radiation hazard to astronauts during extravehicular activity and yields an increased probability of single-event upsets in satellites. In addition, the >100 MeV proton flux exceeding 1 pfu, suggesting an energetic solar particle event, is used as another threshold, marking conditions associated with increased astronaut radiation exposure even inside spacecraft shielding. In the following SEP flux comparisons, we focus on these two operational energy channels when evaluating SOFIE’s predictive performance against GOES observations.

### 3 The SOFIE Model

SOFIE is an integrated solar corona–interplanetary medium–CME–SEP model suite, with the schematic diagram in [Figure 1](#) describing its workflow. Built within the Space Weather Modeling Framework (SWMF, [Tóth et al., 2005, 2012](#); [Gombosi et al., 2021](#)), SOFIE integrates four main components: (1) the Alfvén Wave Solar atmosphere Model-Realtime (AWSoM-R, [van der Holst et al., 2014](#); [I. V. Sokolov et al., 2013, 2021](#)), solving stream-aligned magnetohydrodynamic (MHD) equations ([I. V. Sokolov et al., 2022](#)), designed for simulating the ambient solar wind with reliable magnetic connectivity; (2) the Eruptive Event Generator with the Gibson-Low magnetic configuration (EEGGL, [Gibson & Low, 1998](#); [Borovikov et al., 2017](#); [Jin et al., 2017](#)) for CME generation and propagation; (3) the Multiple Field-Line-Advection Model for Particle Acceleration (M-FLAMPA, [I. V. Sokolov et al., 2004](#); [Borovikov et al., 2018](#); [Liu, Sokolov, et al., 2025](#)), used to simulate particle acceleration and transport processes; and (4) the Particle ARi-

zona and Michigan Solver on Advected Nodes (PARMISAN, X. Chen et al., 2025), a Monte-Carlo solver for SEPs. While PARMISAN is a test-particle code that needs more than millions of test particles for good statistics, M-FLAMPA directly solves the canonical distribution function of SEPs from the Parker transport equation (Parker, 1965). In M-FLAMPA, the advecting effect of solar wind flows, adiabatic cooling/heating, and parallel diffusion are incorporated, while the cross-field diffusion and particle drift (gradient, curvature, and current sheet drift) effects are neglected, with particle transport calculated along individual magnetic field lines only. Although this simplification limits the treatment of lateral transport across field lines, it allows M-FLAMPA to efficiently simulate particle acceleration at CME-driven shocks and the subsequent transport process, which is suitable for operational predictions. Hence, we used the first three components of SOFIE in the testbed exercise, as presented in Figure 1. A comprehensive description of the SOFIE model is available in Zhao et al. (2024) and Liu, Sokolov, et al. (2025).

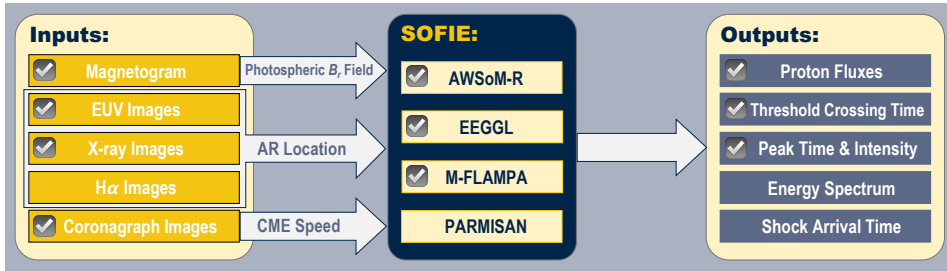


**Figure 1.** Schematic diagram of the prototyped SOFIE model suite (middle), as well as its inputs (left) and SEP outputs (right). Items with a marker were used in the SWPT exercise.

To simulate an SEP event, a magnetogram, which provides the photospheric radial magnetic field ( $B_r$ ), is taken as input for AWSoM-R to simulate the three-dimensional (3D) global solar wind background. In AWSoM-R, the Poynting flux parameter serves as the primary free parameter for tuning the background solar wind, which depends on the phase of the solar cycle and is adjusted in operations based on Equation (1) in Huang et al. (2024). When a CME eruption is observed, the extreme-ultraviolet (EUV), X-ray, or  $H\alpha$  images are typically used to provide the active region (AR) location, with EUV and X-ray images adopted for this purpose in the testbed exercise. We also used coronagraph images to estimate the CME speed. The EEGGL module then combines the magnetogram, AR location, and CME speed to generate the CME flux rope, which is subsequently propagated in AWSoM-R MHD simulations, with M-FLAMPA modeling

the resulting SEP fluxes simultaneously. In M-FLAMPA, there are mainly two free parameters: (1) the seed particle scaling factor, which sets the injected particle population at the shock front with a default value of 1.0 and can be adjusted to better reproduce observed profiles, when the SEP peak intensity is observed; and (2) the upstream mean free path parameter (see Equation (15) in Liu, Sokolov, et al., 2025), which affects particle acceleration, transport and the resulting time–intensity profiles, and was set as 0.1 astronomical units (au) for both events during the SWPT exercise. Detailed discussions of their impacts and uncertainties are provided in Section 6.3.

From these coupled simulations, SOFIE provides the two-dimensional (2D) proton flux distribution on a Sun-centered sphere at a specified radial distance, threshold crossing time of operational channels, peak time and intensity, energy spectrum and shock arrival time, etc. In the testbed exercise, we show the 2D distribution on the 1 au sphere and extract the time–intensity profile along Earth’s trajectory. In Table 1, we list the SOFIE input parameters used in the testbed exercise and further discuss them in Sections 4 and 5 below.

**Table 1.** Input parameters of the AWSOM-R, EEGGL, and M-FLAMPA models in SOFIE for the SWPT exercise simulation.

Model	Input Parameter	Provider	Value for the Eruptive Event on	
			10 September 2017	4 November 2001
AWSOM-R	Poynting flux parameter	Modeler	0.55 MW m <sup>-2</sup> T <sup>-1</sup>	0.20 MW m <sup>-2</sup> T <sup>-1</sup>
EEGGL	AR location <sup>a</sup>	SWPC	S12W85	N05W24
	CME speed	M2M SWAO	2650 km s <sup>-1</sup>	1925 km s <sup>-1</sup>
M-FLAMPA	Injection scaling factor	Modeler	1.0	10.0
	Mean free path parameter <sup>b</sup>	Modeler	0.1 au	0.1 au

<sup>a</sup> These locations are given in Stonyhurst heliographic longitude and latitude.

<sup>b</sup> This corresponds to  $\lambda_0$  of Equation (15) in Liu, Sokolov, et al. (2025).

## 4 The 10 September 2017 Event

During the testbed exercise, we first simulated the solar radiation storm condition based on the 10 September 2017 SEP event. In the following, we describe how we prepared the steady-state solar wind background and simulated the CME and SEP fluxes on-site during the SWPT exercise.

### 4.1 Steady-State Solar Wind Simulation

The steady-state solar wind simulation was prepared in advance of the SWPT exercise. For the 10 September 2017 event, we used the hourly updated, zero-point corrected synoptic map from the Global Oscillation Network Group of the National Solar Observatory (NSO/GONG, [Harvey et al., 1996](#); [Hill, 2018](#)). Figure 2(a) shows the input GONG synoptic map incorporating magnetograms up to 15:04 universal time (UT) on 10 September 2017, right before the solar eruptive event. This synoptic map has a resolution of  $1^\circ$  in longitude and latitude, corresponding to a  $360 \times 180$  grid covering the entire solar surface. We increase the  $B_r$  magnitude in its weak-field regions using Equation (1) of [Liu, Sokolov, et al. \(2025\)](#). Driven by the processed synoptic map and a Poynting flux parameter of  $0.55 \text{ MW m}^{-2} \text{ T}^{-1}$ , the stream-aligned AWSoM-R was run in advance to calculate the steady-state solar wind parameters for a period of 27 days centered at this time. For this event, the AWSoM-R steady-state solution required  $\sim 3$  hours of simulation time on 25 Intel Cascade Lake nodes of the NASA Pleiades supercomputer, each with two 20-core Intel Xeon Gold 6248 processors, for a total of 1,000 central processing unit (CPU) cores. This timing highlights the operational motivation for preparing the background solar wind in advance. This preparation is also briefly discussed and summarized below in Section 7.

In this simulation, we use a block-adaptive 3D spherical grid in the solar corona (SC) domain (1.1–24 solar radii,  $R_s$ ) and a block-adaptive Cartesian cubic grid in the inner heliosphere (IH) domain (20–650  $R_s$ ) that encloses the SC domain, with an overlapping buffer grid between 20 and 24  $R_s$  that couples the SC and IH solutions. In the SC, the angular resolution is initially set as 1.4 degrees. Within  $r = 1.7 R_s$ , the angular resolution is increased by one level to 0.7 degrees (see the grid resolution in yellow near the Sun in Figure 2(b)), while it is coarsened by one level to 2.8 degrees outside of this radial range. Adaptive mesh refinement (AMR, [Gombosi et al., 2003](#); [Tóth et al.,](#)

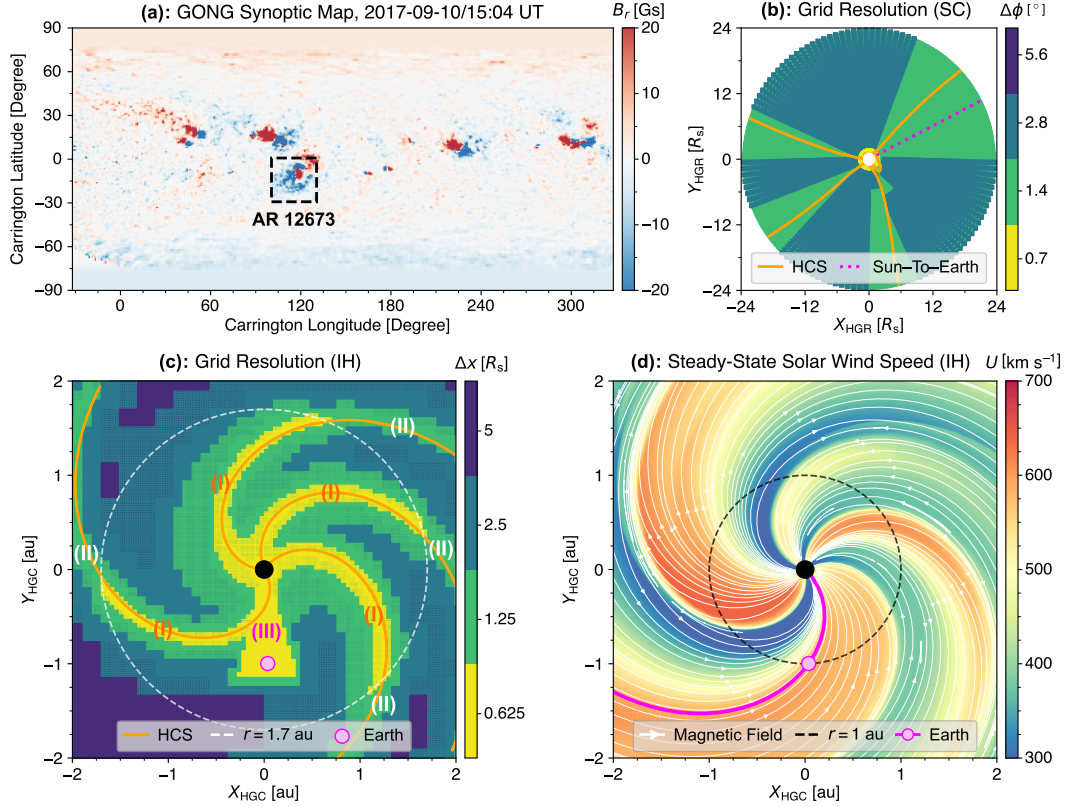


**Figure 2.** The input photospheric synoptic map and the steady-state solar wind solutions for the 10 September 2017 event. (a) Input GONG synoptic map including observations up to 15:04 UT on 10 September 2017, with the black dashed box marking the parent AR (NOAA AR 12673) for this event. (b) Angular grid resolution ( $\Delta\phi$ ) of the steady-state simulation in the SC ecliptic plane in heliographic rotating (HGR) coordinates. The white solid circle at the center denotes the inner boundary of the SC domain at a heliocentric distance ( $r$ ) of  $1.1 R_s$ . The HCS is plotted as orange lines, and the Sun-to-Earth connection line is plotted as a magenta dashed line. (c) Mesh size ( $\Delta x$ ) of the steady-state simulation in the IH ecliptic plane in Carrington heliographic (HGEC) coordinates. The black solid circle at the center denotes the inner boundary of the IH domain at  $r = 20 R_s$ , and the white dashed circle marks the IH shell at  $r = 1.7 \text{ au}$ . The HCS is marked as orange lines. Multiple AMR criteria are indicated as: (I) HCS refinement within the IH shell, (II) HCS refinement beyond the IH shell, and (III) Earth-directed cone refinement. (d) Steady-state solar wind speed in the IH ecliptic plane in HGEC coordinates. Multiple white curves with arrows indicate magnetic field lines, with the Earth-connected field line highlighted in magenta. The black solid and dashed circles represent heliocentric distances of  $20 R_s$  and  $1 \text{ au}$ , respectively.

2012) is applied in both domains to refine the heliospheric current sheet (HCS) and later along the CME propagation direction, ensuring that key coronal and heliospheric structures are adequately resolved. In addition, AMR is applied along an Earth-directed cone to better resolve the solar wind and CME structures most relevant to near-Earth space weather. This grid setup is referred to as Setup 1 for the discussion in Section 6.2.

Figure 2(b)(c) illustrates the grid resolution in the ecliptic plane within the SC and IH domains, respectively, showing regions of enhanced resolution applied to the HCS, the Earth-directed cone, and specific radial shells of  $r = 1.7 R_s$  in SC and 1.7 au in IH. In Figure 2(d), we show the simulated steady-state solar wind speed in the solar ecliptic plane in IH, plotted with Earth and its connected magnetic field line. We also plot other magnetic field lines as white curves with arrows, demonstrating the alignment between the magnetic field and the solar wind plasma stream (see also I. V. Sokolov et al., 2022; Wraback et al., 2024; X. Chen et al., 2025).

## 4.2 CME Generation and Propagation

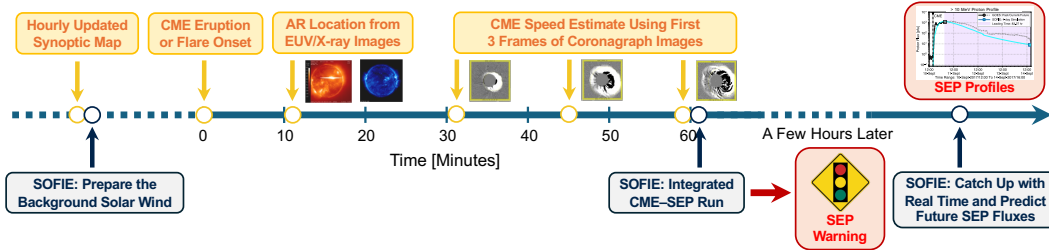


**Figure 3.** Schematic timeline of the SOFIE workflow under simulated operational conditions for one SEP event. The observational inputs of SOFIE, as shown in Figure 1, and their corresponding available time are illustrated in yellow boxes above the time axis. Key steps for modeling an SEP event by SOFIE in the SWPT exercise, including preparation of the background solar wind and the integrated CME–SEP simulation under simulated operational conditions, are illustrated in blue boxes below the time axis. The resulting SEP flux profile predictions and warnings, illustrated in red boxes, are issued typically a few hours after the eruption, which varies from event to event.

After preparing steady-state solar wind solutions, we awaited information about the AR location and CME speed during the testbed exercise. At 15:35 UT on 10 September 2017, an X-ray flare was first observed by SWPC forecasters, originating from NOAA

AR 12673 at Stonyhurst heliographic latitude  $-12^\circ$  and longitude  $+85^\circ$  (S12W85) as viewed from Earth. The flare peaked at  $\sim 15:52$  UT with an intensity corresponding to the X8.2 class. Shortly afterwards, at 16:00 UT, the associated CME first appeared in the SOHO/Large Angle and Spectrometric Coronagraph (LASCO, described in [Brueckner et al., 1995](#)) images. During the exercise, we waited until three consecutive LASCO frames were available, allowing a reasonably confident estimate of the CME speed, reported as  $2650 \text{ km s}^{-1}$  by M2M SWAO analysts using the SWPC-CAT. Although M2M SWAO analysts' CME speed determinations were used as model inputs in this study, this selection was made for consistency within the collaborative nature of this exercise but does not represent the formal operational workflow for real-time CME forecasting, in which CME speeds are normally provided by SWPC forecasters. The current data pipeline in NOAA/SWPC typically incurs a  $\sim 10$ -minute delay to determine the source AR location, depending on the imagery cadence, and it took about 1 hour to obtain the CME speed after the CME eruption. Details about this 1-hour delay are discussed in [Section 6.1](#). [Figure 3](#) provides a schematic timeline summarizing the operational workflow for each event in the SWPT exercise, particularly during the early onset phase, including the CME eruption time, data availability, model initiation, and the forecast window. Details about the runtime and efficiency of SOFIE throughout the SEP event are described later in [Sections 4.3, 5.3, and 6.2](#).

Then, we used the synoptic map, AR location, and CME speed as inputs (see [Table 1](#)) for EEGGL to parameterize the CME flux rope. As shown in [Figure 4\(a\)](#), we inserted the resulting force-imbalanced spheromak-type magnetic flux rope and its entrained plasma on top of the parent AR (NOAA AR 12673 for this event). For both events in the SWPT exercise, SOFIE was run on-site using 1,000 CPU cores of Intel Cascade Lake nodes.

The modeled synthetic white-light (WL) images are compared with LASCO observations at 16:11 UT on 10 September 2017, as shown in [Figure 4\(b\)\(c\)](#). These images represent the region from 2 to  $6 R_s$  within the LASCO/C2 field of view, with the inner black circle denoting an occultation disk at  $2 R_s$ . The color scale represents the relative change in WL total brightness with respect to the steady-state solar wind background. Here, both the observation and the simulation show the CME propagating westward, with the bright leading front reaching a comparable distance of  $\sim 6 R_s$  in the plane of the sky

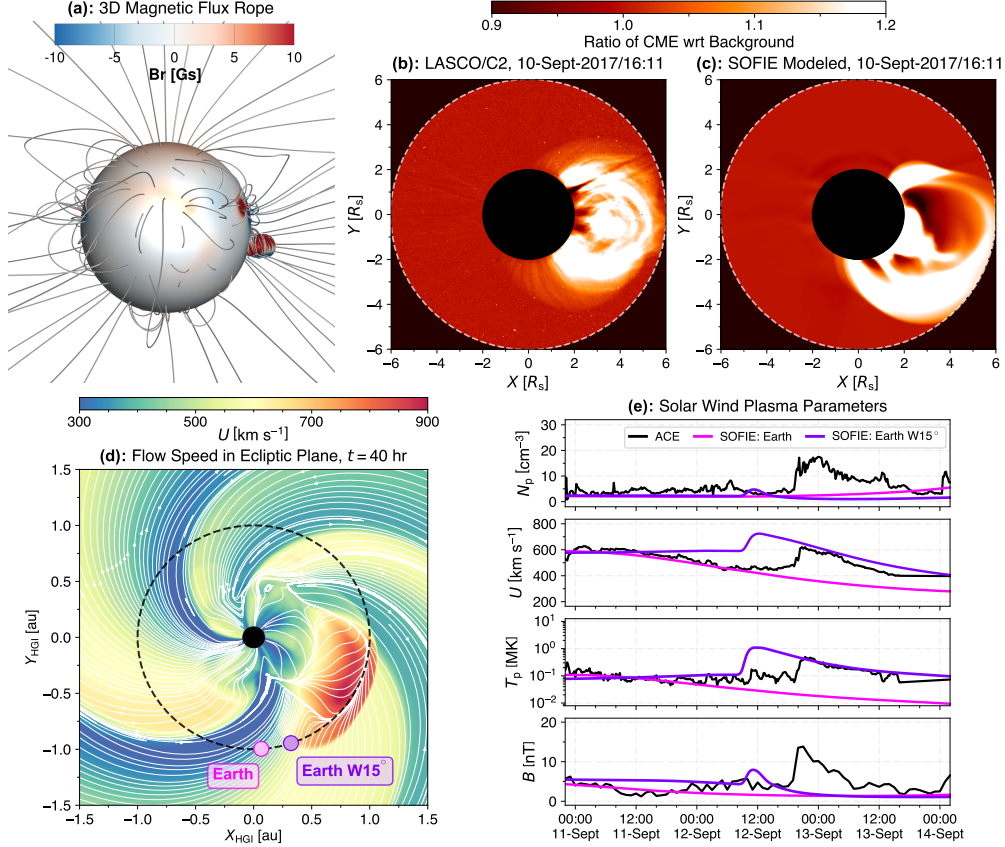


**Figure 4.** CME simulation results during the 10 September 2017 event. Panel (a) shows the initial 3D CME flux rope inserted above the parent AR at the inner boundary of the SC domain ( $r = 1.1 R_s$ ), viewed from Earth and colored by the radial magnetic field strength ( $B_r$ ). Panels (b)–(c) show the LASCO/C2 observation and SOFIE-synthesized WL images at 16:11 UT on 10 September 2017. The color scale indicates the relative change in WL total brightness, expressed as the ratio of the CME signal to the background solar wind before the eruption. In both panels, the field of view is limited within  $r = 6 R_s$ , with the central black solid circle marking an occultation disk at  $r = 2 R_s$ . Panel (d) shows the flow speed in the IH ecliptic plane in heliographic inertial (HGI) coordinates, 40 hours after the eruption, when the ICME flank approaches Earth. Multiple magnetic field lines are marked as white curves with arrows, and a black dashed circle denotes the heliocentric distance of 1 au. The magenta and purple scatter points denote Earth and its  $15^\circ$  westward position in the ecliptic plane, respectively. Panel (e) shows the modeled solar wind plasma parameters at Earth (in magenta) and its  $15^\circ$  westward position in the ecliptic plane (in purple), together with ACE observations at Earth (in black). Parameters shown from top to bottom are the plasma number density ( $N_p$ ), solar wind speed ( $U$ ), plasma temperature ( $T_p$ ), and magnetic field strength ( $B$ ).

at this time. The simulated results also clearly exhibit the classic three-part CME morphology (e.g., Illing & Hundhausen, 1985).

As the CME propagates outward and evolves into an interplanetary CME (ICME), the shock flank approaches Earth about 40 hours after the eruption. Figure 4(d) shows the solar wind speed with magnetic field lines in the IH ecliptic plane at this time. In the simulation, the ICME flank extends toward Earth but does not directly impact it, likely because of the presence of the HCS acting as an obstacle and Earth’s location  $\sim 90^\circ$  in longitude away from the source AR. To better examine the solar wind properties at the flank, we consider a reference position  $15^\circ$  westward of Earth in the ecliptic plane. Figure 4(e) compares the simulated solar wind plasma parameters at these two locations with the ACE *in situ* observations at Earth. In observations, the shock arrived at  $\sim 20:00$  UT on 12 September, whereas the simulated ICME does not reach Earth. At the  $15^\circ$  westward position, the simulated ICME shock front arrived 8–10 hours earlier than observed by ACE, with a comparable solar wind speed and ion temperature, but lower plasma density and magnetic field strength. In our simulation, we find that the CME/ICME is significantly deflected as a result of interaction with the HCS and the stream interaction region in the background solar wind. We also note that the choice of both steady-state model and flux-rope parameters can impact the simulated plasma and magnetic properties of the CME (e.g., Jivani et al., 2023; Huang et al., 2024; H. Chen et al., 2025). However, in this study for simulated real-time operations, we do not explore varying the model parameters.

### 4.3 SEP Distribution and Fluxes

As the AWSOM-R MHD simulation was initiated on-site during the SWPT exercise, M-FLAMPA simultaneously solved the distribution function of energetic protons along magnetic field lines, providing both spatial and temporal characteristics about the SEP distribution. Figure 5(a)(b) illustrates the modeled  $>10$  MeV and  $>100$  MeV proton fluxes on the 1 au sphere 10 hours after the launch of the CME flux rope. In each panel, the Earth’s location and the CME flux rope footpoint on the Sun’s surface are marked as “E” in a magenta circle and “F” in a green square, respectively. We can find obvious longitudinal and latitudinal variations of the energetic proton fluxes. In the  $>10$  MeV channel (Figure 5(a)), proton fluxes can reach as high as  $10^4$  pfu, and in the  $>100$  MeV channel (Figure 5(b)) they can reach  $\sim 10^3$  pfu, concentrated on the 1 au sphere

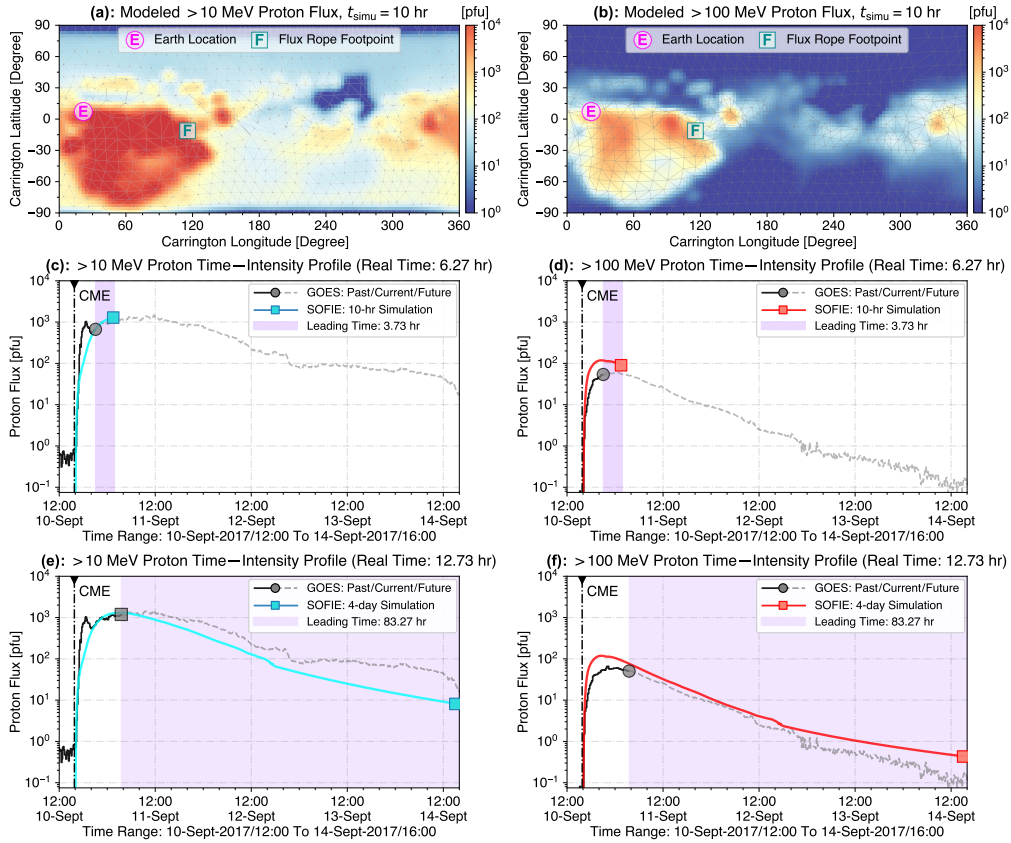


**Figure 5.** Distribution of energetic protons in the 10 September 2017 event. Panels (a) and (b) show SOFIE-modeled fluxes of  $>10$  MeV and  $>100$  MeV protons, respectively, on a logarithmic scale on the 1 au sphere, 10 hours after the eruption. In each panel, the  $x$ - and  $y$ -axes are Carrington longitude and latitude, respectively. The thin gray vertices correspond to the field line intersections with the 1 au sphere, and the edges indicate the triangulation skeleton constructed via the Delaunay triangulation approach (Delaunay, 1934; Lee & Schachter, 1980). The Earth’s location is marked as “E” in a magenta circle, and the CME flux rope footpoint on the solar surface is marked as “F” in a green square. Panels (c) and (d) show the  $>10$  MeV and  $>100$  MeV proton time–intensity profiles at Earth, respectively, 6.27 real-time hours after the eruption, corresponding to the time when SOFIE predicts 10-hour proton fluxes. In each panel, GOES observations are plotted as a black curve, followed by a dark gray circle and a light gray curve indicating past, current, and future fluxes, respectively. SOFIE results are plotted as cyan and red curves with square markers, representing the  $>10$  MeV and  $>100$  MeV energy channels, respectively. A dashed-dotted vertical line represents the CME eruption time, and a vertical purple band marks the prediction leading time of 3.73 hours, also indicated in the legend. Panels (e) and (f) are similar to panels (c) and (d), but 12.73 real-time hours after the eruption, when SOFIE predicts 4-day proton fluxes, yielding a leading time of 83.27 hours.

primarily within  $0^{\circ}$ – $120^{\circ}$  east of the flux rope footpoint. In contrast, on the 1 au sphere, regions  $45^{\circ}$ – $180^{\circ}$  west of the flux rope, corresponding to the backside of CME propagation, barely exhibit SEPs, with fluxes 2–4 orders of magnitude lower. These spatial variations illustrate the critical role of large-scale magnetic connectivity between the CME-driven shock and the observer: regions with favorable connectivity experience substantially higher SEP fluxes, while poorly connected regions receive minimal fluxes (see also, e.g., Cane et al., 1988; Lario et al., 2013, 2017).

Figure 5(c)–(d) shows the modeled and observed proton time–intensity profiles at Earth, 6.27 real-time hours after the eruption, when SOFIE provides 10-hour proton flux predictions. Here, the real time is counted since the flare onset and incorporates the  $\sim 1$ -hour delay for obtaining CME information as SOFIE inputs. The GOES observations are plotted as black and gray curves, representing the past, current, and future fluxes, respectively. The SOFIE-predicted  $>10$  MeV and  $>100$  MeV proton fluxes are shown as cyan and red curves with square markers. At this moment, the GOES observed proton fluxes were still increasing toward their peak, while SOFIE already reproduced comparable onset and peak fluxes within a factor of 2, with a prediction leading time of 3.73 hours, defined hereafter as the difference between the simulation time and the real time, and also used as a model performance metric.

The SEP time–intensity profiles at Earth from the completed 4-day SOFIE simulation are presented in Figure 5(e)–(f) using the same plot style. Overall, the modeled profiles show very good agreement with the GOES observations, from the onset and peak to decay, and in terms of time and fluxes. Specifically, in this event, a magnetic cloud has been reported to pass Earth  $\sim 2$  days after the eruption (see Figure 4(e) and J. Guo et al., 2018; Luhmann et al., 2018). For SEPs observed by GOES, this interval corresponds to a small plateau in the  $>10$  MeV channel and a modest drop thereafter in both the  $>10$  MeV and  $>100$  MeV channels around 20:00 UT on 12 September 2017. In the simulation, a similar decrease was reproduced but occurred about 4–5 hours earlier than observed, mainly because the modeled ICME flank approached Earth earlier (see Figure 4(d)(e)), although the CME/ICME arrival at Earth is not perfectly captured in the *in situ* solar wind plasma comparison. Although the simulated ICME did not reach Earth directly, the connectivity between Earth and the CME/ICME-driven shock could have changed. Nonetheless, this timing discrepancy is relatively minor compared to the  $\gtrsim 4$ -day duration of this event, particularly given that the interplanetary shock did not pro-

duce a strong enhancement of energetic storm particles (ESPs) in this case. Notably, the 4-day SOFIE simulation completed within 13 hours of real time, at a point when the observed fluxes were still near their peak or just beginning to decay, providing the full forecast profile up to 4 days in advance.

During the SWPT exercise, we were allocated 4–6 hours to test the operational workflow for each event. Within this limited time, SOFIE was able to provide only the first several hours of predictions. Specifically, SOFIE predicted the threshold crossing time for  $>10$  MeV,  $>10$  pfu 1.46 hours after the flare onset (1 hour for the input delay, plus 0.46 hours of running time), and for  $>100$  MeV,  $>1$  pfu 1.26 hours after the flare onset. However, the GOES observation reported corresponding threshold crossing times 57 and 27 minutes after the flare onset, respectively, indicating that the earliest SEP threshold warnings from SOFIE lagged the first observed threshold crossing by  $\sim 1$  hour in real time. For this event simulation, we also find that SOFIE caught up with the real time after 3.21 hours, again suggesting a delay of the earliest forecast of SEP flux warning. Here, we note that the most time-consuming part of the simulation lies in the SC domain, where the grid size is small (on the order of  $10^{-2}$ – $10^{-1} R_s$ ) and the MHD characteristic wave speeds are high (hundreds of  $\text{km s}^{-1}$ ), thereby requiring very small global time steps (on the order of  $10^{-1}$  s). As the CME flux rope propagates outward from the SC domain into the IH, the simulation progressively becomes faster due to coarser grid spacing and lower characteristic speeds (see also Figure 10 and associated texts for the change in runtime speed). In-depth discussions with forecasters, operators, and analysts on-site in the SWPT exercise led to a practical suggestion and test, which is to coarsen the grid in the SC domain by a factor of two and evaluate the impact on both accuracy and speed in the next event simulation.

## 5 The 4 November 2001 Event

On the second day of the SWPT exercise, we simulated the solar eruptive event on 4 November 2001. We describe the approach for preparation, simulation and SOFIE results for this event similar to Section 4.

### 5.1 Steady-State Solar Wind Simulation

With the feedback from the first event simulation (see the end of Section 4.3), we coarsened the grid in SC by a factor of two (referred to as Setup 2 hereafter) when we prepared the background solar wind. Since GONG magnetograms are only accessible after September 2006, we used a zero-point corrected, Carrington rotation (CR) synoptic map based on the SOHO/Michelson Doppler Imager (MDI, Scherrer et al., 1995) observations. Figure 6(a) shows the input MDI synoptic map, integrated over CR 1982 from 17 October to 13 November 2001. It has a resolution of  $0.1^\circ$  in longitude and  $0.125^\circ$  in latitude, corresponding to a  $3600 \times 1440$  grid covering the entire solar surface. We remap it to a  $360 \times 180$  grid with  $1^\circ$  resolution in both longitude and latitude and amplify  $B_r$  in the weak-field regions using Equation (1) of Liu, Sokolov, et al. (2025). The global magnetic field strength during this period is notably stronger than that in September 2017 (see Figure 2(a)), consistent with the fact that this SEP event occurs near the solar cycle 23 maximum. We prepared the steady-state solar wind plasma over this CR using a Poynting flux parameter of  $0.2 \text{ MW m}^{-2} \text{ T}^{-1}$  in AWSoM-R, which required approximately 1–1.5 hours of simulation time on 1,000 CPU cores even for this coarser grid setup.

In Figure 6(b)(c), we show the grid resolution in the SC and IH domains, respectively. Compared with the mesh setup in the previous event (Figure 2(b)(c)), the overall angular resolution in the SC is coarsened by a factor of 2, and the mesh size for the heliospheric structures in the IH remains the same. In Figure 6(d), we plot the simulated steady-state solar wind speed in the ecliptic plane in the IH domain using the same style as in Figure 2(d). The results again demonstrate the resolved heliospheric structure and the expected alignment between the magnetic field and the solar wind flow, and show the global ambient solar wind background into which the CME and SEPs are subsequently simulated to propagate.

### 5.2 CME Generation and Propagation

During the testbed exercise, we monitored solar activity using real-time data. At 16:09 UT on 4 November 2001, SWPC forecasters reported an X-ray flare erupting from NOAA AR 9684 at N05W24 as viewed from Earth, which peaked around 16:18 UT with an X1.0-class intensity. Shortly after, a fast-halo CME was first detected by LASCO/C2

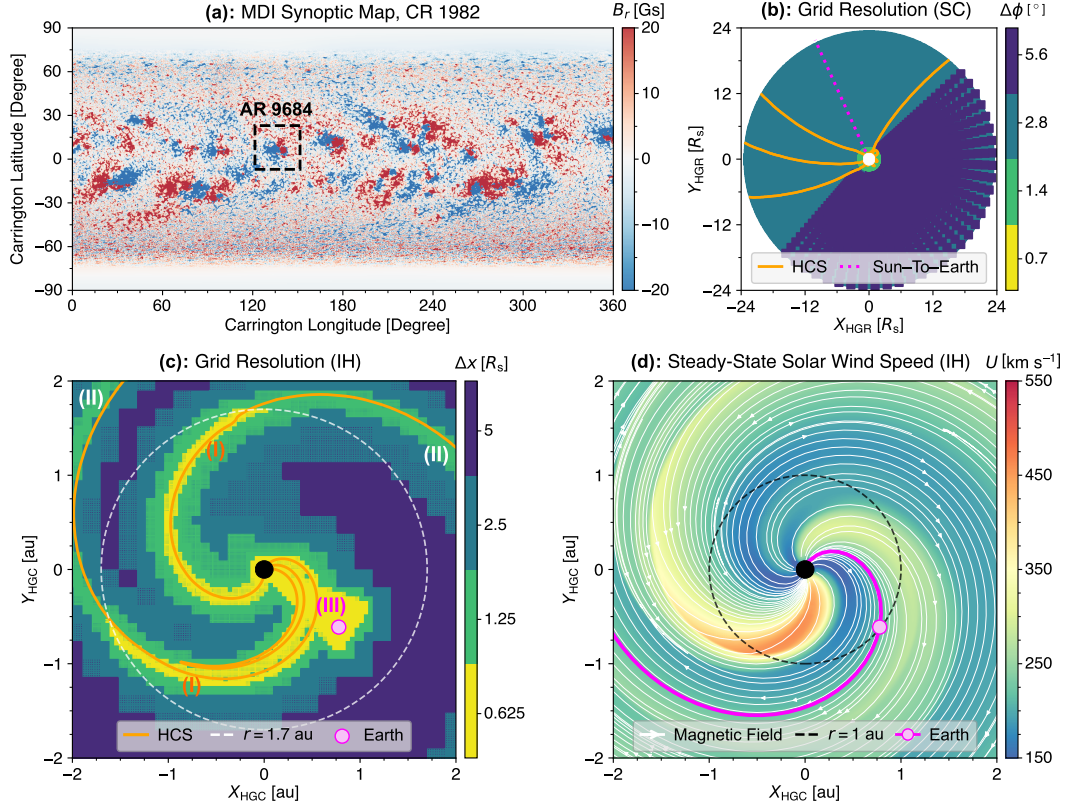


**Figure 6.** The input photospheric synoptic map, the angular resolution of the grid in the SC, the mesh size in the IH, and the steady-state solar wind solutions in the IH for the 4 November 2001 event, shown in panels (a)–(d), respectively, with the same plot style as Figure 2 except for adjusted plotting ranges and ticks.

at 16:35 UT. After three consecutive LASCO frames became available, which is  $\sim 1$  hour after the flare onset, a plane-of-sky CME speed of  $1925 \text{ km s}^{-1}$  was provided by the M2M SWAO analysts using the SWPC-CAT. Taking the MDI synoptic map, together with the identified AR location and CME speed listed in Table 1, we generated the CME flux rope via EEGGL and placed it above the parent AR (see Figure 7(a)).

We show the WL images from the LASCO/C2 coronagraph and SOFIE simulations at 16:53 UT on 4 November 2001. The LASCO/C2 observation in Figure 7(b) shows a halo CME propagating predominantly westward, with its bright core extending northward. The corresponding SOFIE-synthesized WL image in Figure 7(c) reproduces the overall flux rope structure, also appearing as a westward-directed halo CME that reaches approximately the same radial distance ( $6 R_s$ ) as observed.

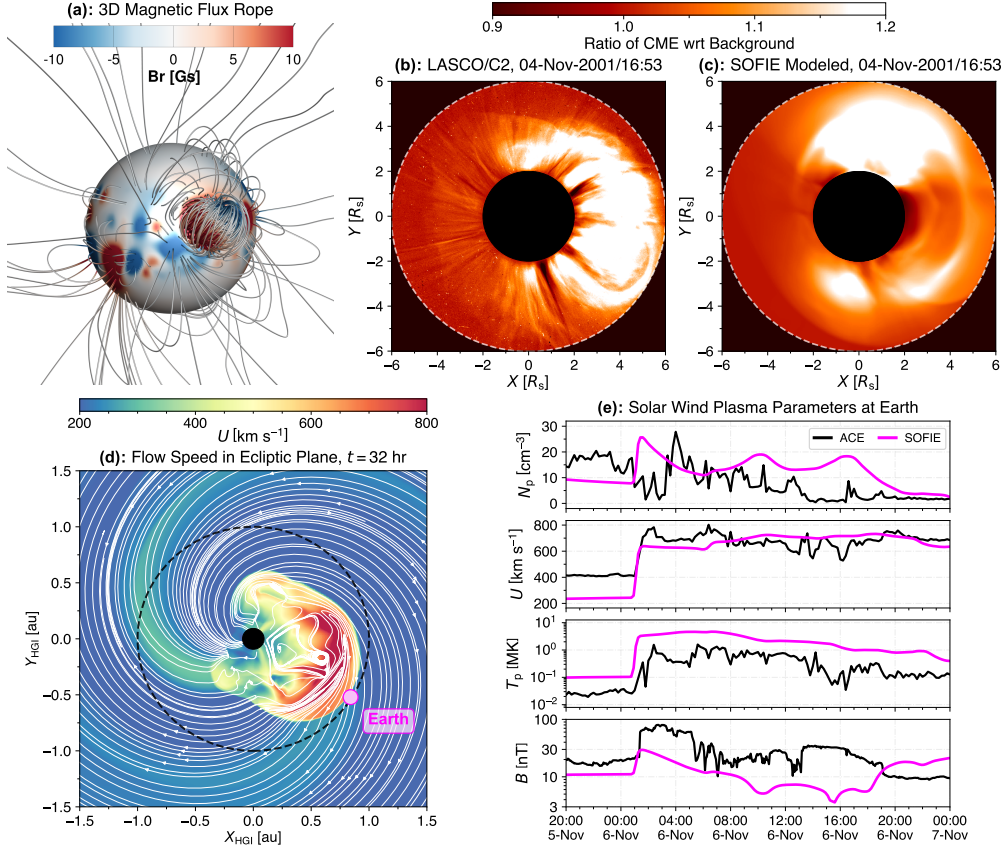


**Figure 7.** CME generation and propagation results during the 4 November 2001 event, including the initial 3D CME flux rope in panel (a); the observed and simulated LASCO/C2 WL images at 16:53 UT on 4 November 2001 shown in panels (b)–(c); the flow speed in the IH ecliptic plane ecliptic shown in panel (d); and the solar wind plasma parameters at Earth in panel (e), presented in the same plot style as Figure 4, except for detailed plotting ranges and ticks.

As the CME propagates from the SC to the IH domain evolving into an ICME, the CME-driven shock arrives at Earth 32 hours after the eruption. Figure 7(d) shows the solar wind speed, together with multiple magnetic field lines, in the ecliptic plane at this time. As shown, the ICME is directed toward Earth, with its shock front impacting Earth and a sheath region followed by the magnetic cloud. In Figure 7(e), we compare the solar wind plasma parameters at Earth from ACE *in situ* observations and SOFIE simulations, which are overall in good agreement. The shock arrival time,  $\sim$ 01:30 UT on 6 November 2001, aligns well between ACE observations and SOFIE simulations. The amplitudes of the solar wind speed, plasma number density, and temperature after the shock arrival also agree well. While ACE observes the peak of the magnetic field am-

plitude of  $\sim 80$  nT, SOFIE predicts about 30 nT. This is a typical amplitude for ICME-driven shocks arriving at Earth in AWSOM/EEGGL simulations (e.g., Manchester et al., 2004; Jin et al., 2017; H. Chen et al., 2025). We also note several CMEs occurred in the days preceding this event (Kuznetsov et al., 2003; Shen et al., 2008). As this large CME propagates outwards, it can interact or merge with the earlier CMEs/ICMEs, resulting in an enhanced magnetic field amplitude at 1 au as observed by ACE. However, since the present analysis focuses on the major event during the testbed exercise, those preceding CMEs were not included in the simulation, which could have distorted the solar wind background and accounted for the differences in the comparison above.

### 5.3 SEP Distribution and Fluxes

As the simulated CME propagates, M-FLAMPA outputs the distribution function of the energetic protons along multiple field lines. Figure 8 illustrates the resulting spatial distribution and temporal evolution of energetic protons during the 4 November 2001 SEP event, following the same plotting pattern as Figure 5. Similarly, in Figure 8(a)(b), we plot the modeled proton fluxes at energies  $>10$  MeV and  $>100$  MeV on the 1 au sphere, 10 hours after the eruption, showing broad variations of the SEP fluxes in longitudes and latitudes. These spatial variations again highlight that SEP fluxes are primarily determined by the global magnetic connectivity and shock properties. While local plasma conditions may not be perfectly reproduced in Figure 7(e), which results in some timing and amplitude offsets during the ESP phase at Earth, the SOFIE model can still provide a physically plausible representation of the global SEP distribution throughout the inner heliosphere (Figure 8(a)–(b)) and overall reasonable agreement with SEP observations at Earth (Figure 8(d)–(f)).

The  $>10$  MeV and  $>100$  MeV proton time–intensity profiles at Earth are presented in Figure 8(c)–(f), following the same plot style as Figure 5(c)–(f). We show the profiles for 10 and 96 simulated hours after the eruption in panels (c)(d) and (e)(f), corresponding to 2.35 and 4.86 real-time hours after the eruption, respectively. Both observed and simulated proton fluxes rise rapidly after the CME eruption. For the  $>10$  MeV channel, SOFIE/M-FLAMPA predicts an onset peak of  $\gtrsim 1,000$  pfu, in close agreement with the GOES observation of  $\sim 3,000$  pfu within a factor of 2–3. In the  $>100$  MeV channel, SOFIE/M-FLAMPA gives a higher peak of  $\sim 100$  pfu, compared to the  $\sim 40$  pfu measured by GOES. In this simulation, SOFIE provided the SEP threshold crossing time

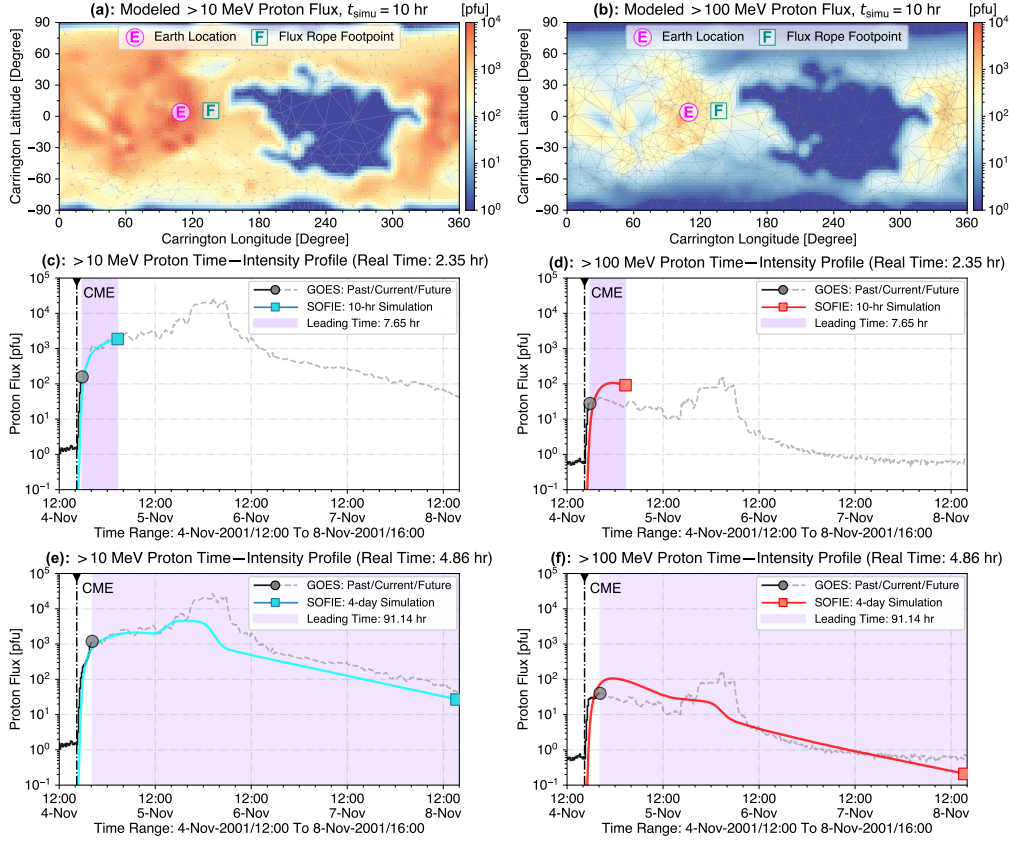


**Figure 8.** Distribution of energetic protons during the 4 November 2001 event, including the modeled >10 MeV and >100 MeV proton fluxes on the 1 au sphere at 10 hours after the eruption shown in panels (a)–(b), and the proton time–intensity profiles shown in panels (c)–(f), plotted in the same style as Figure 5 except for adjusted plotting ranges and ticks.

prediction with a delay of  $\lesssim 0.6$  hours with respect to the GOES observations for both energy channels (see Setup 2 in Table 2), as the simulation was initiated after CME inputs became available  $\sim 1$  hour after the eruption. A more detailed assessment of SOFIE’s operational timing and latency is presented in Section 6.2.

In this event, a strong ICME-driven shock propagates toward Earth, accelerating the particles locally but over a shorter transport distance to Earth. After 12:00 UT on 5 November 2001, we can find a second enhancement in both > 10 MeV and >100 MeV proton fluxes observed by GOES, which is the ESP peak and coincides with the ICME shock passage later at  $\sim 01:30$  UT on 6 November. In the simulation, the main features of these two energy channels are basically reproduced, although both profiles maintain lower plateaus. This difference implies that the shock may have remained stronger than

predicted in interplanetary space, and that the diffusive nature of the simulation (especially under the reduced spatial resolution) and the preceding CMEs/ICMEs not included in our SWPT simulations could have played a role in shaping the ESP phase.

Overall, the SOFIE/M-FLAMPA simulation captures the main characteristics of this intense SEP event, especially the amplitude and timing of the SEP onset and ESP peak, despite some detailed deviations in the time–intensity profile. In particular, using a coarser grid setup in the SC domain for this event simulation, we can predict the 4-day profile in 5 hours of real time, which showcases the operational usefulness of the SOFIE model.

## 6 Discussion

### 6.1 Coronagraph Latency and Forecast Timeliness Considerations

For the two SEP events simulated during the SWPT exercise, we adopted an input latency of  $\sim 1$  hour for the CME speed estimation as the SOFIE input (see Figure 3). In fact, this  $\sim 1$ -hour delay accounts for the latency of  $\sim 20$ – $30$  minutes for the availability of the first coronagraph images used to estimate CME kinematics under nominal conditions, together with the additional time required to obtain three consecutive images for the CME speed estimate. While this latency assumption might represent an optimistic real-world case during the SWPT exercise, it is consistent with current operational practices. In particular, the GOES-19 Compact Coronagraph 1 (CCOR-1) instrument (<https://ccor.nrl.navy.mil/>, Thernisien et al., 2025), launched in 2024, represents a major advancement in space weather predictions as the first operational coronagraph, which affords a latency of  $\sim 30$  minutes from image capture until availability to SWPC forecasters and a cadence of 15 minutes. While this 1-hour input delay corresponds to the historic nominal operational scenario (see <https://lasco-www.nrl.navy.mil/index.php?p=content%2Frealtime> and <https://www.swpc.noaa.gov/>), we acknowledge that, historically, latencies in real-world varied depending on data availability and quality control procedures, and that additional processing or coordination steps introduced additional delays (e.g., Posner et al., 2014). With the deployment of CCOR-1, these latencies have been drastically reduced reliably to  $\lesssim 30$  minutes.

## 6.2 Impacts of Grid Resolution on SEP Prediction Accuracy and Timing

While SOFIE was run on a coarser grid setup for the SC domain (Setup 2) described in Section 4.3, we also used the default grid configuration (Setup 1), as described in Section 4.1, to run SOFIE after the SWPT exercise. In addition, on-site in the SWPT exercise, interactive discussions were held among the CLEAR team and SWPC forecasters, SRAG console operators, and M2M SWAO analysts, suggesting a grid setup that maintains the coarser grid resolution for the background as in Setup 2 and keeps the default resolution for the HCS, as well as CME-faced and Earth-oriented cones (Setup 3). We then used these grid setups to run SOFIE and conducted a comparative study in terms of the SEP prediction accuracy and timing.

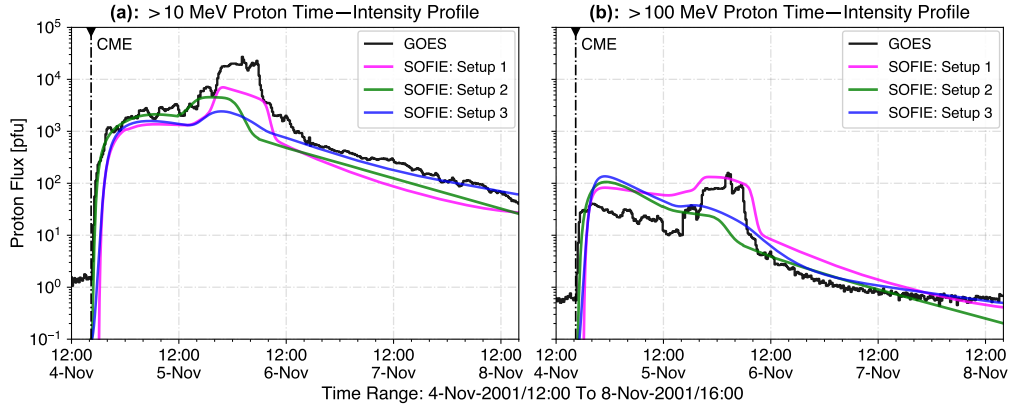


**Figure 9.** Comparison of the (a)  $>10$  MeV and (b)  $>100$  MeV proton time–intensity profiles at Earth observed by GOES (in black) and simulated by SOFIE based on different grid setups (in magenta, green, and blue) in the 4 November 2001 event. A dashed-dotted vertical line marks the launch of the CME in each panel. Detailed explanations of the simulation grid setup are described in text.

In Figure 9, we compare the  $>10$  MeV and  $>100$  MeV proton time–intensity profiles between the GOES observations (black) and the SOFIE simulation results based on three grid configurations, Setups 1–3 (magenta, green, and blue, respectively). Across all three runs, both the SEP onset phase during the first day after the eruption and the decay phase after 12:00 UT on 6 November show good agreement with GOES observations. Among them, Setup 1 exhibits the best overall consistency, particularly in reproducing the ESP-phase timing and peak intensity. In contrast, Setup 2, which was run

on-site during the SWPT exercise, shows an earlier ESP-phase onset and a smaller peak amplitude. This discrepancy likely arises from the coarser grid resolution in SC, which results in a more diffusive CME evolution. Setup 3, although maintaining finer resolution near the HCS and along the CME- and Earth-directed regions, still produces a slightly reduced ESP-phase peak compared with Setup 1.

In Figure 10, we present the simulation runtime of SOFIE using 1,000 CPU cores based on the three grid setups. Panel (a) shows that all runs complete the 4-day simulation faster than in real time, particularly after  $\sim 12$  hours of simulated time. The steepening of the runtime curves after 12 hours of simulated time reflects the changing physical regime throughout the event. Early in the simulation, small grid cells and high fast magnetosonic speeds in the SC domain require small global time steps and frequent SC–IH coupling (30 seconds), as well as short time steps in M-FLAMPA during active shock acceleration. After 12 hours of simulated time, the CME flux rope has largely exited the SC domain and entered the IH domain, the coupling interval is increased to 15 minutes and both MHD and particle time steps increase, substantially reducing the computational cost. Panel (b) provides a zoomed-in view of the first 12 hours in real time, where the intersections between the SOFIE runtime curves and the real-time reference indicate when the SOFIE simulations catch up with real time, with the  $\sim 1$ -hour delay for obtaining CME input parameters accounted for. We find that Setup 2 reaches this point within 1.19 hours of real time, i.e., 0.19 hours after the simulation starts, while Setups 1 and 3 catch up after 10.87 and 4.11 hours of real time, respectively. As shown here, together with Sections 4.3 and 5.3, while the earliest SEP forecast, typically the onset phase, is delayed by a couple of hours due to computational and input latency constraints, SOFIE can still predict the multi-day evolution of SEP fluxes, the decay-phase characteristics, and ESP-phase particle fluxes, providing valuable guidance for the subsequent evolution throughout the SEP event. While we consider two extreme SEP events in the SWPT exercise with sharp particle flux enhancements, the typical time from flare rise or CME onset to SEP threshold crossing ranges from  $\sim 1$  hour to several hours (e.g., Papaioannou et al., 2016; Kahler et al., 2017; Liu et al., 2023, 2024); in this situation, the effective latency in the earliest SEP forecasts produced by SOFIE is generally smaller, including for the threshold crossing time, onset peak time, and peak intensity.

Moreover, based on the simulation results and runtimes for the 4 November 2001 event, Table 2 details the threshold crossing time, the onset peak time and intensity, and

**Table 2.** Comparison between observations and SOFIE predictions using different grid resolution setups in the 4 November 2001 event.

		4 November 2001 Event			
Item		Observation	Setup 1	Setup 2	Setup 3
>10 MeV Protons	Threshold Crossing Time	2001-11-04T17:05	2001-11-04T18:37	<b>2001-11-04T17:11</b>	2001-11-04T18:25
	In Real Time*	0.93 hr	3.92 hr	<b>1.13 hr</b>	2.53 hr
	Leading Time of SOFIE	–	–2.99 hr	<b>–0.20 hr</b>	–1.60 hr
	Onset Peak Time	2001-11-05T04:45	2001-11-05T07:03	2001-11-05T06:33	<b>2001-11-05T05:29</b>
	Onset Peak Intensity	2,804 pfu	1,369 pfu	<b>2,126 pfu</b>	1,579 pfu
	In Real Time*	12.60 hr	12.82 hr	<b>2.75 hr</b>	9.79 hr
	Leading Time of SOFIE	–	–0.22 hr	<b>+9.85 hr</b>	+2.81 hr
	ESP Phase Peak Time	2001-11-06T02:20	<b>2001-11-05T21:53</b>	2001-11-05T18:55	2001-11-05T21:31
	ESP Phase Peak Intensity	27,149 pfu	<b>7,021 pfu</b>	4,535 pfu	2,421 pfu
	In Real Time*	34.18 hr	14.55 hr	<b>3.13 hr</b>	11.78 hr
	Leading Time of SOFIE	–	+19.63 hr	<b>+31.05 hr</b>	+22.40 hr
	Spearman Correlation Coefficient	–	<b>0.9293</b>	0.8410	0.8681
	Percentage within an Order of Magnitude	–	<b>99.87%</b>	92.66%	84.68%
	Percentage within a Factor of 2	–	<b>41.73%</b>	37.71%	37.66%
Median Logarithmic Error	–	–0.1828	0.0542	<b>–0.0350</b>	
Median Absolute Logarithmic Error	–	<b>0.3323</b>	0.4137	0.4055	
>100 MeV Protons	Threshold Crossing Time	2001-11-04T16:45	2001-11-04T18:25	<b>2001-11-04T17:11</b>	2001-11-04T18:01
	In Real Time*	0.60 hr	3.77 hr	<b>1.13 hr</b>	2.24 hr
	Leading Time of SOFIE	–	–3.17 hr	<b>–0.53 hr</b>	–1.64 hr
	Onset Peak Time	2001-11-04T20:40	<b>2001-11-04T22:55</b>	2001-11-04T23:11	<b>2001-11-04T22:55</b>
	Onset Peak Intensity	41 pfu	<b>82 pfu</b>	106 pfu	136 pfu
	In Real Time*	4.52 hr	7.39 hr	<b>1.98 hr</b>	5.83 hr
	Leading Time of SOFIE	–	–2.87 hr	<b>+2.54 hr</b>	–1.31 hr
	ESP Phase Peak Time	2001-11-06T02:25	<b>2001-11-05T22:09</b>	2001-11-05T16:27	2001-11-05T18:41
	ESP Phase Peak Intensity	162 pfu	<b>132 pfu</b>	28 pfu	38 pfu
	In Real Time*	34.27 hr	14.58 hr	<b>3.06 hr</b>	11.42 hr
	Leading Time of SOFIE	–	+19.69 hr	<b>+31.21 hr</b>	+22.85 hr
	Spearman Correlation Coefficient	–	<b>0.9178</b>	0.5628	0.5716
	Percentage within an Order of Magnitude	–	<b>99.63%</b>	92.09%	97.81%
	Percentage within a Factor of 2	–	41.69%	<b>49.22%</b>	46.74%
Median Logarithmic Error	–	0.3431	<b>0.1299</b>	0.2136	
Median Absolute Logarithmic Error	–	0.3563	<b>0.3029</b>	0.3615	
Real Time to Provide 4-day Proton Fluxes	96.00 hr	21.12 hr	<b>4.86 hr</b>	18.57 hr	
Leading Time of SOFIE	–	+74.88 hr	<b>+91.14 hr</b>	+77.43 hr	
When can SOFIE catch up with real time?	–	10.87 hr	<b>1.19 hr</b>	4.11 hr	

*Note.* The three simulation setups listed in the header correspond to different grid resolution configurations, as described in text. Items marked with \* indicate the real time when each result was obtained, representing the elapsed time since the flare onset (2001-11-04T16:09). The prediction leading time is calculated as the difference between the real time at which the simulation result was obtained and the corresponding observation time. A positive value indicates that SOFIE ran faster than real time, and vice versa. For each grid setup and energy channel, we use multiple metrics to evaluate the overall time–intensity profile, and include the moment when the SOFIE simulation time caught up with the real time. Besides, for each item, the optimal result or shortest timing among the three setups is highlighted in bold.

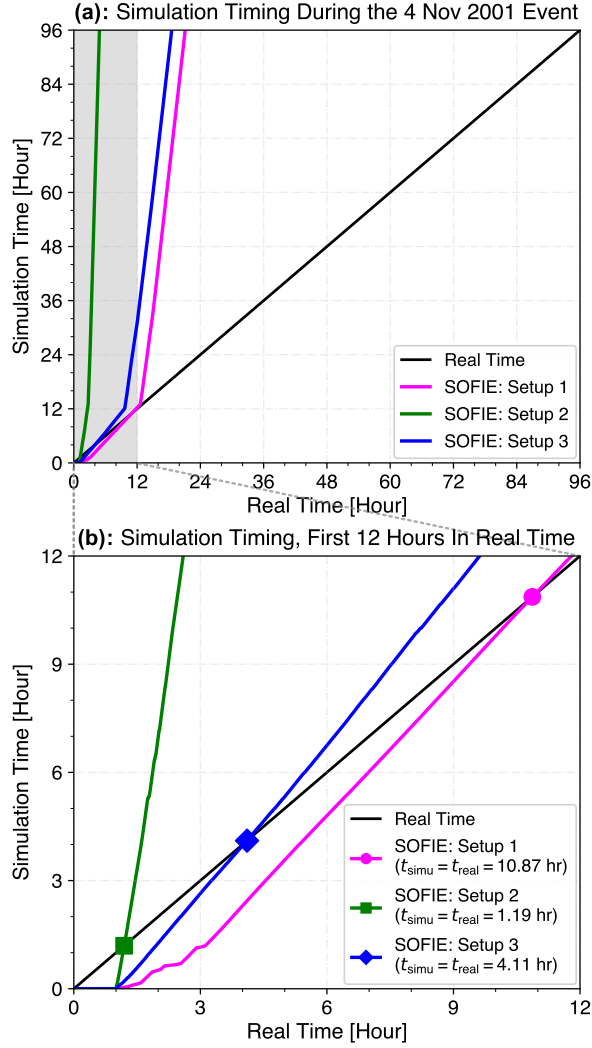


**Figure 10.** Simulation timing of SOFIE during the 4 November 2001 SEP event. (a) The overall timing profile over a 4-day window in real time. (b) A zoomed-in view of the first 12 hours in real time. In both panels, the  $x$ - and  $y$ -axes represent real time and simulation time, respectively. The magenta, green, and blue curves correspond to SOFIE runtimes based on Setups 1–3, while the black diagonal line represents the real-time reference. In panel (b), the magenta dot, green square, and blue diamond mark the moments when the SOFIE simulation time catches up with real time for the respective setups, with the exact time labeled in the legend. Note that all simulations start after 1 hour of real time, due to the delay in obtaining CME input parameters.

the ESP phase peak time and intensity in the  $>10$  MeV and  $>100$  MeV proton fluxes as measured by GOES and simulated by SOFIE under Setups 1–3. For both energy chan-

nels, five statistical metrics commonly used in SEP model validation (e.g., Whitman et al., 2023, 2024, 2026, and <https://ccmc.gsfc.nasa.gov/challenges/sep/validation/>) are also calculated to evaluate the 4-day time profiles. Additionally, we list the real time when GOES observed or SOFIE predicted each item. In the following, we summarize the key findings from the comparison for the 4 November 2001 event.

1. Overall, Setup 1 provides the best agreement with GOES observations, particularly in reproducing the ESP phase, although it requires  $\sim 21$  hours to complete the 4-day prediction. Specifically, it achieves a point-to-point Spearman correlation coefficient  $>0.9$ , with  $>99\%$  of data points within an order of magnitude and about  $42\%$  within a factor of 2 of the GOES measurements.
2. Setup 2 runs substantially faster than real time ( $\sim 5$  hours), while achieving comparable accuracy and capturing the main temporal and intensity trends. Compared with the other two setups, Setup 2 exhibits a noticeably reduced delay in reproducing the early SEP threshold crossings and reaches the modeled onset peak several hours earlier in real time.  $\sim 92\%$  of its data points fall within an order of magnitude and  $\sim 40\%$  ( $38\%$  for  $>10$  MeV and  $49\%$  for  $>100$  MeV protons) within a factor of 2 of the GOES observed data.
3. Setup 3 performs moderately between the two in terms of runtime. For the 4 November 2001 event presented here, results based on Setup 3 are slightly better in some metrics, but are typically intermediate or show larger deviations from the GOES measurements than Setups 1 and 2. Its minimal global time step is comparable to that of Setup 1, explaining the similar completion time for the 4-day simulation. However, its coarser background grid resolution, as used in Setup 2, reduces the accuracy of CME and SEP predictions.
4. For all setups, the  $>10$  MeV predictions exhibit a bias (median logarithmic error) close to zero, suggesting that the predicted values are generally centered around the GOES observations. In contrast, the  $>100$  MeV predictions show a positive bias, primarily due to the overestimation of the onset peak as shown in Figure 9(b). The aggregated accuracy (median absolute logarithmic error) is similar among all setups, indicating that half of the predicted data points fall within about one-third of an order of magnitude of GOES measurements.

These results demonstrate that all three setups are capable of providing operationally useful forecasts, with Setup 1 offering higher accuracy and Setup 2 providing timely, operationally referencing predictions that can operate significantly faster than real time. Based on the comparison above, for human space missions like Artemis II, it is recommended to run Setups 1 and 2 simultaneously: Setup 2 provides a good order-of-magnitude estimate of the SEP event within a couple of hours, while Setup 1 increases the accuracy. Setup 2 should be used in the first  $\sim 5$  hours or so, and Setup 1 will take over afterwards. Nevertheless, further validation studies and event-by-event analysis should be conducted to provide generic suggestions on the grid resolution configuration used for operations.

### 6.3 Uncertainties in Predicted Results

Although SOFIE has been applied to multiple historical SEP events (Zhao et al., 2024) and tested under simulated operational conditions during the SWPT exercise, some deviations from observations remain. For the three components within SOFIE, we list their input free parameters used in this work in Table 1, respectively. Uncertainties of the predicted SEP fluxes may arise from these input parameters, such as the background solar wind based on parameter tuning for historical events and the CME input parameters. Although not explored here, assessing the sensitivity of SOFIE’s SEP predictions to variations in CME parameters, such as those derived from different sources (e.g., SWPC, M2M SWAO, or LASCO catalog), would be valuable for quantifying model robustness and guiding its future operational implementation (see also Mays et al., 2015; Richardson et al., 2015; Papaioannou, Vasalos, et al., 2025). In the following, we focus our discussion on the free input parameters used in M-FLAMPA and their influence on the accuracy and reliability of the predicted results.

In M-FLAMPA, seed particles are estimated following the suprathermal tail of the solar wind and injected uniformly at the shock front using a scaling factor. This scaling factor is a free parameter set as 1.0 by default, which can be highly affected by the properties of the CME-driven shock (see Section 4.5 in Zhao et al., 2024, for its physical interpretations). In practice, it may need to be fine-tuned to reproduce measured SEP fluxes. For example, we adopted a scaling factor of 10 for the 4 November 2001 event in the SWPT exercise to better reproduce the GOES measurements. Because this parameter primarily controls the overall particle intensity level, its effective value is typ-

ically constrained when the SEP onset peak is issued. Together with the delayed availability of the first forecast in the initial hours, this represents a current operational limitation. Nevertheless, once constrained, the model provides valuable information on the subsequent evolution of SEP intensities, decay-phase characteristics, and particle fluxes during the ESP phase. For operational predictions, however, a more robust estimate of seed particle populations injected into the particle acceleration process (e.g., Zank et al., 2000; F. Guo & Giacalone, 2013; Caprioli & Spitkovsky, 2014; Afanasiev et al., 2015) is needed and essential to improve the predictive capability of SEPs in the future.

Another free parameter in M-FLAMPA is the parallel mean free path parameter of SEPs in the upstream solar wind, which affects both particle acceleration at the shock and subsequent transport processes. Variations in this parameter can alter the predicted threshold crossing time, peak intensity, decay phase profile, and particle energy spectrum (see Figure 9 in Zhao et al. (2024), Figure 15 in Liu, Sokolov, et al. (2025), Els et al. (2024); Lang et al. (2024); Zhong et al. (2024), and references therein). In the SWPT exercise, we used the same value of 0.1 au for both events (see Table 1), although the optimal value may differ for individual events. In the future, we plan to simulate a larger set of historical events during the SOFIE validation phase, allowing this free parameter to be adjusted based on historical event statistics or empirical relations to improve forecast reliability for operational predictions.

In the current configuration of M-FLAMPA, we also note that cross-field diffusion and particle drift effects are neglected (see Section 3 and references therein), such that SEP transport is restricted to individual magnetic field lines. As a result, uncertainties in magnetic connectivity (e.g., the event shown in Figure 4(e)) can further influence the predicted SEP fluxes. Under these assumptions, the parallel mean free path mentioned here should be regarded as an effective parameter rather than a direct representation of the physical scattering conditions when additional transport processes are included. While addressing these limitations will require further model development, ensemble simulations and probabilistic estimates of the mean free path represent promising refinements to improve forecast robustness and reliability for current operational applications.

## 7 Summary and Conclusion

As SEPs can pose significant space radiation hazards, it is crucial to provide a timely prediction of their fluxes at any location in interplanetary space for upcoming human exploration missions. The physics-based models can play an important role for this purpose. In this work, we describe the simulated operational testing of SOFIE, a physics-based SEP model developed in the CLEAR Space Weather Center of Excellence, and demonstrate its performance in the 2025 SWPT exercise at NOAA/SWPC.

Designed to predict SEP fluxes, SOFIE self-consistently integrates models that simulate the ambient solar wind, parameterize CME flux ropes, and solve shock-driven particle acceleration and transport processes. During the SWPT exercise, SOFIE was tested under simulated operational conditions for two historical SEP events, the 10 September 2017 and 4 November 2001 eruptions. For the 10 September 2017 event, we used the default grid configuration previously employed in [Zhao et al. \(2024\)](#) and [Liu, Sokolov, et al. \(2025\)](#), where SOFIE could provide accurate 4-day SEP predictions within 13 hours of real time. For the 4 November 2001 event, based on in-depth discussions with analysts and operators from SWPC, CCMC, SRAG, and M2M SWAO, we coarsened the grid in the SC by a factor of 2 and performed on-site simulations at the SWPT. Running on 1,000 CPU cores, SOFIE reproduced key features of the observed CME coronagraph images and SEP fluxes, and was able to deliver 4-day predictions in only 5 hours, which is significantly faster than real time. Note that for both events, we prepared the background solar wind in advance, and the corresponding timing is not included. For operational use, the steady-state solar wind has been simulated every day through an established pipeline (<https://solarwind.engin.umich.edu/current/>, [I. Sokolov et al., 2025](#)) driven by the most up-to-date GONG photospheric synoptic map. When a CME is detected, we can restart the simulation from the latest available background solar wind. While we acknowledge that the solar wind can evolve within a 24-hour window and that preceding CMEs may modify the heliospheric background and magnetic connectivity (e.g., [Manchester et al., 2017](#); [Zhuang et al., 2020](#)), a detailed assessment of these effects is beyond the scope of the present study and will be addressed in future work, including the use of a shorter and computationally affordable cadence of background update. Moreover, interactive discussions on-site at the SWPT also suggested coarsening only the background grid in the SC domain while retaining the finer resolution of the HCS, CME path, and Earth-directed regions as the default setup. Therefore, we conducted post-exercise

simulations and comparisons among three grid setups, showing that the default grid achieves the highest accuracy, while the coarser grid adopted on-site during the SWPT exercise offers timely, decision-oriented predictions in applications.

These results for the SWPT exercise demonstrate that the physics-based SEP model, SOFIE, traditionally viewed as computationally expensive, can in fact meet the latency and robustness requirements of operational predictions. With continued validation and integration into model forecasting, SOFIE represents a significant step toward the real-time, physics-based SEP prediction in support of future human space exploration.

### Open Research Section

The GONG and MDI synoptic maps used in this work are available on <https://gong.nso.edu/data/magmap/> and [http://jsoc.stanford.edu/MDI/MDI\\_Magnetograms.html](http://jsoc.stanford.edu/MDI/MDI_Magnetograms.html), respectively. The SOHO/LASCO WL image data are obtained using SolarSoftWare (SSW, <https://www.lmsal.com/solarsoft/>), which downloads original data through the Virtual Solar Observatory (VSO, <https://sdac.virtualsolar.org/cgi/search>) and accounts for the instrumental calibration. The *in situ* ACE solar wind plasma and magnetic field parameters used in this study are accessible on <https://izw1.caltech.edu/ACE/ASC/level2/index.html>. The GOES SEP data are obtained from <https://www.ncei.noaa.gov/data/goes-space-environment-monitor/access/avg/>. The SWMF/SOFIE is available on <https://github.com/SWMFsoftware>, and the SOFIE model can be run via run-on-request ([https://ccmc.gsfc.nasa.gov/ror/requests/SH/SWMF-AWSom/swmfawsom\\_user\\_registration.php](https://ccmc.gsfc.nasa.gov/ror/requests/SH/SWMF-AWSom/swmfawsom_user_registration.php)) at CCMC. All observation and simulation data shown in plots, including the 2D ecliptic plane data, time series of solar wind plasma parameters along Earth's trajectory, 3D solar wind plasma and magnetic field data right after flux rope insertion, WL image data, and 2D distributions and time-intensity profiles of energetic protons, are publicly available on the Zenodo platform (Liu, Zhao, et al., 2025).

### Conflict of Interest

The authors declare that there are no conflicts of interest for this study.

### Acknowledgments

The authors sincerely thank the two anonymous reviewers for their time and effort devoted to improving this paper. This work is supported by NASA Living With a Star (LWS)

Strategic Capability project under NASA grant 80NSSC22K0892 (SCEPTER), NASA Space Weather Center of Excellence program under award 80NSSC23M0191 (CLEAR), NSF grant GEO-2149771 (ANSWERS), NASA grant 80NSSC21K1124, and NASA LWS grant 80NSSC20K1778. The authors express their great gratitude to the SOHO project, an international cooperation between European Space Agency (ESA) and NASA, the GOES and ACE teams, and also the NSO Integrated Synoptic Program. The authors also thank Dr. Yang Liu from Stanford University for providing assistance with the MDI magnetogram data. Computational resources supporting this work are provided by the NASA High-End Computing (HEC) Program through the NASA Advanced Supercomputing (NAS) Division at the Ames Research Center (<https://www.nas.nasa.gov/hecc/>), and the high-performance computing support from the Texas Advanced Computing Center (TACC) Frontera at the University of Texas at Austin (<https://tacc.utexas.edu/>, Stanzione et al., 2020). Any opinions, findings, conclusions or recommendations expressed in this material are those of the authors and do not necessarily reflect the views of the participating agencies or affiliated institutions.

## References

- Afanasiev, A., Battarbee, M., & Vainio, R. (2015). Self-consistent Monte Carlo simulations of proton acceleration in coronal shocks: Effect of anisotropic pitch-angle scattering of particles. *Astronomy & Astrophysics*, *584*, A81. doi: 10.1051/0004-6361/201526750
- Anastasiadis, A., Lario, D., Papaioannou, A., Kouloumvakos, A., & Vourlidis, A. (2019). Solar energetic particles in the inner heliosphere: status and open questions. *Philosophical Transactions of the Royal Society A*, *377*(2148), 20180100. doi: 10.1098/rsta.2018.0100
- Bain, H. M., Copeland, K., Onsager, T. G., & Steenburgh, R. A. (2023). NOAA Space Weather Prediction Center Radiation Advisories for the International Civil Aviation Organization. *Space Weather*, *21*(7), e2022SW003346. doi: 10.1029/2022SW003346
- Borovikov, D., Sokolov, I., Roussev, I., Taktakishvili, A., & Gombosi, T. (2018). Toward a quantitative model for simulation and forecast of solar energetic particle production during gradual events. I. Magnetohydrodynamic background coupled to the SEP Model. *The Astrophysical Journal*, *864*(1), 88. doi:

- 10.3847/1538-4357/aad68d
- Borovikov, D., Sokolov, I. V., Manchester, W., Jin, M., & Gombosi, T. I. (2017). Eruptive event generator based on the Gibson-Low magnetic configuration. *Journal of Geophysical Research: Space Physics*, *122*(8), 7979–7984. doi: 10.1002/2017JA024304
- Brueckner, G. E., Howard, R. A., Koomen, M. J., Korendyke, C. M., Michels, D. J., Moses, J. D., ... Eyles, C. J. (1995, December). The Large Angle Spectroscopic Coronagraph (LASCO). *Solar Physics*, *162*(1-2), 357-402. doi: 10.1007/BF00733434
- Buzulukova, N., & Tsurutani, B. (2022). Space weather: From solar origins to risks and hazards evolving in time. *Frontiers in Astronomy and Space Sciences*, *9*, 1017103. doi: 10.3389/fspas.2022.1017103
- Cane, H., Reames, D., & Von Rosenvinge, T. (1988). The Role of Interplanetary Shocks in the Longitude Distribution of Solar Energetic Particles. *Journal of Geophysical Research: Space Physics*, *93*(A9), 9555–9567. doi: 10.1029/JA093iA09p09555
- Caprioli, D., & Spitkovsky, A. (2014). Simulations of ion acceleration at non-relativistic shocks. I. Acceleration efficiency. *The Astrophysical Journal*, *783*(2), 91. doi: 10.1088/0004-637X/783/2/91
- Chen, H., Sachdeva, N., Huang, Z., van der Holst, B., Manchester IV, W., Jivani, A., ... Toth, G. (2025). Decent Estimate of CME Arrival Time From a Data-Assimilated Ensemble in the Alfvén Wave Solar Atmosphere Model (DECADE-AWSOM). *Space Weather*, *23*(1), e2024SW004165. doi: 10.1029/2024SW004165
- Chen, X., Zhao, L., Giacalone, J., Sachdeva, N., Sokolov, I. V., Toth, G., ... others (2025). Evidence of Time-dependent Diffusive Shock Acceleration in the 2022 September 5 Solar Energetic Particle Event. *The Astrophysical Journal*, *994*(2), 242. doi: 10.3847/1538-4357/ae1227
- Delaunay, B. (1934). Sur la sphère vide. a la mémoire de georges voronoï. *Bull. Acad. Science USSR VII: Class. Sci. Mat. Nat.*(6), 793–800. Retrieved from <https://www.mathnet.ru/links/95d7c8aa6111426eaf4114db10ced544/im4937.pdf>
- Desai, M., & Giacalone, J. (2016). Large Gradual Solar Energetic Particle Events.

- Living Reviews in Solar Physics*, 13(1), 3. Retrieved from <https://doi.org/10.1007/s41116-016-0002-5> doi: 10.1007/s41116-016-0002-5
- Els, P., Engelbrecht, N., Lang, J., & Strauss, R. (2024). The Diffusion Tensor of Protons at 1 au: Comparing Simulation, Observation, and Theory. *The Astrophysical Journal*, 975(1), 134. doi: 10.3847/1538-4357/ad7c44
- Georgoulis, M. K., Yardley, S. L., Guerra, J. A., Murray, S. A., Ahmadzadeh, A., Anastasiadis, A., ... others (2024). Prediction of solar energetic events impacting space weather conditions. *Advances in Space Research*. doi: 10.1016/j.asr.2024.02.030
- Gibson, S. E., & Low, B. (1998). A Time-dependent Three-dimensional Magnetohydrodynamic Model of the Coronal Mass Ejection. *The Astrophysical Journal*, 493(1), 460. doi: 10.1086/305107
- Gombosi, T. I., Chen, Y., Glocer, A., Huang, Z., Jia, X., Liemohn, M. W., ... others (2021). What Sustained Multi-disciplinary Research can Achieve: The Space Weather Modeling Framework. *Journal of Space Weather and Space Climate*, 11, 42. doi: 10.1051/swsc/2021020
- Gombosi, T. I., De Zeeuw, D. L., Powell, K. G., Ridley, A. J., Sokolov, I. V., Stout, Q. F., & Tóth, G. (2003). Adaptive mesh refinement for global magnetohydrodynamic simulation. *Space Plasma Simulation*, 247–274. Retrieved from [https://doi.org/10.1007/3-540-36530-3\\_12](https://doi.org/10.1007/3-540-36530-3_12) doi: 10.1007/3-540-36530-3.12
- Guo, F., & Giacalone, J. (2013). The Acceleration of Thermal Protons at Parallel Collisionless Shocks: Three-dimensional Hybrid Simulations. *The Astrophysical Journal*, 773(2), 158. doi: 10.1088/0004-637X/773/2/158
- Guo, J., Dumbović, M., Wimmer-Schweingruber, R. F., Temmer, M., Lohf, H., Wang, Y., ... others (2018). Modeling the evolution and propagation of 10 September 2017 CMEs and SEPs arriving at Mars constrained by remote sensing and in situ measurement. *Space Weather*, 16(8), 1156–1169. doi: 10.1029/2018SW001973
- Guo, J., Wang, B., Whitman, K., Plainaki, C., Zhao, L., Bain, H. M., ... others (2024). Particle radiation environment in the heliosphere: Status, limitations, and recommendations. *Advances in Space Research*. doi: 10.1016/j.asr.2024.03.070

- Guo, J., Zeitlin, C., Wimmer-Schweingruber, R. F., Hassler, D. M., Ehresmann, B., Rafkin, S., ... Wang, Y. (2021). Radiation environment for future human exploration on the surface of Mars: the current understanding based on MSL/RAD dose measurements. *Astronomy and Astrophysics Reviews*, *29*, 1–81. doi: 10.1007/s00159-021-00136-5
- Harvey, J., Hill, F., Hubbard, R., Kennedy, J., Leibacher, J., Pintar, J., ... others (1996). The global oscillation network group (GONG) project. *Science*, *272*(5266), 1284–1286. Retrieved from <https://doi.org/10.1126/science.272.5266.1284> doi: 10.1126/science.272.5266.1284
- Hill, F. (2018). The Global Oscillation Network Group Facility—an Example of Research to Operations in Space Weather. *Space Weather*, *16*(10), 1488–1497. doi: 10.1029/2018SW002001
- Huang, Z., Tóth, G., Sachdeva, N., & van der Holst, B. (2024). Solar Wind Driven from GONG Magnetograms in the Last Solar Cycle. *The Astrophysical Journal*, *965*(1), 1. doi: 10.3847/1538-4357/ad32ca
- Illing, R., & Hundhausen, A. (1985). Observation of a coronal transient from 1.2 to 6 solar radii. *Journal of Geophysical Research: Space Physics*, *90*(A1), 275–282. Retrieved from <https://doi.org/10.1029/JA090iA01p00275> doi: 10.1029/JA090iA01p00275
- Jin, M., Manchester, W., van der Holst, B., Sokolov, I., Tóth, G., Mullinix, R., ... Gombosi, T. (2017). Data-constrained coronal mass ejections in a global magnetohydrodynamics model. *The Astrophysical Journal*, *834*(2), 173. doi: 10.3847/1538-4357/834/2/173
- Jin, M., Manchester, W., van der Holst, B., Sokolov, I., Tóth, G., Vourlidas, A., ... Gombosi, T. (2017). Chromosphere to 1 AU simulation of the 2011 March 7th event: a comprehensive study of coronal mass ejection propagation. *The Astrophysical Journal*, *834*(2), 172. doi: 10.3847/1538-4357/834/2/172
- Jivani, A., Sachdeva, N., Huang, Z., Chen, Y., van der Holst, B., Manchester, W., ... others (2023). Global Sensitivity Analysis and Uncertainty Quantification for Background Solar Wind Using the Alfvén Wave Solar Atmosphere Model. *Space Weather*, *21*(1), e2022SW003262. Retrieved from <https://doi.org/10.1029/2022SW003262> doi: 10.1029/2022SW003262
- Kahler, S. W., White, S. M., & Ling, A. G. (2017). Forecasting  $E > 50$  MeV proton

- events with the proton prediction system (PPS). *Journal of Space Weather and Space Climate*, 7, A27. doi: 10.1051/swsc/2017025
- Klein, K.-L., & Dalla, S. (2017). Acceleration and Propagation of Solar Energetic Particles. *Space Science Reviews*, 212, 1107–1136. doi: 10.1007/s11214-017-0382-4
- Kress, B. T., Rodriguez, J. V., & Onsager, T. G. (2020). The GOES-R space environment in situ suite (SEISS): Measurement of energetic particles in geospace. In *The GOES-R Series* (pp. 243–250). Elsevier. doi: 10.1016/B978-0-12-814327-8.00020-2
- Krittawong, C., Singh, N. K., Scheuring, R. A., Urquieta, E., Bershad, E. M., Macaulay, T. R., ... others (2022). Human Health during Space Travel: State-of-the-Art Review. *Cells*, 12(1), 40. doi: 10.3390/cells12010040
- Kuznetsov, S., Bogomolov, A., Denisov, Y. I., Kordylewski, Z., Kudela, K., Kurt, V., ... others (2003). The Solar Flare of November 4, 2001, and Its Manifestations in Energetic Particles from Coronas-F Data. *Solar System Research*, 37(2), 121–127. Retrieved from <https://doi.org/10.1023/A:1023384425209> doi: 10.1023/A:1023384425209
- Lang, J., Strauss, R., Engelbrecht, N., van den Berg, J., Dresing, N., Ruffolo, D., & Bandyopadhyay, R. (2024). A Detailed Survey of the Parallel Mean Free Path of Solar Energetic Particle Protons and Electrons. *The Astrophysical Journal*, 971(1), 105. doi: 10.3847/1538-4357/ad55c3
- Lario, D., Aran, A., Gómez-Herrero, R., Dresing, N., Heber, B., Ho, G., ... Roelof, E. (2013). Longitudinal and Radial Dependence of Solar Energetic Particle Peak Intensities: STEREO, ACE, SOHO, GOES, and MESSENGER Observations. *The Astrophysical Journal*, 767(1), 41. doi: 10.1088/0004-637X/767/1/41
- Lario, D., Kwon, R.-Y., Riley, P., & Raouafi, N. (2017). On the Link between the Release of Solar Energetic Particles Measured at Widespread Heliolongitudes and the Properties of the Associated Coronal Shocks. *The Astrophysical Journal*, 847(2), 103. doi: 10.3847/1538-4357/aa89e3
- Lee, D.-T., & Schachter, B. J. (1980). Two algorithms for constructing a Delaunay triangulation. *International Journal of Computer & Information Sciences*, 9(3), 219–242. doi: 10.1007/BF00977785

- Liu, W., Richardson, I. G., Bruno, A., Whitman, K., Johnson, A. S., Trintchouk, A., ... Gombosi, T. I. (2024). Solar Energetic Particle Benchmark Dataset in the CLEAR Space Weather Center of Excellence. In *AGU Fall Meeting Abstracts* (Vol. 2024, p. SH43D-2912). Retrieved from <https://agu.confex.com/agu/agu24/meetingapp.cgi/Paper/1643049>
- Liu, W., Sokolov, I. V., Zhao, L., Gombosi, T. I., Sachdeva, N., Chen, X., ... Bain, H. M. (2025). Physics-based Simulation of the 2013 April 11 Solar Energetic Particle Event. *The Astrophysical Journal*, *985*(1), 82. doi: 10.3847/1538-4357/adc4e3
- Liu, W., Zhao, L., Gombosi, T. I., & Chen, Y. (2023). Benchmarking Dataset of Solar Energetic Particle Events: Validation, Analysis and Implications. In *AGU Fall Meeting Abstracts* (Vol. 2023, p. SH51C-2632). Retrieved from <https://agu.confex.com/agu/fm23/meetingapp.cgi/Paper/1377410>
- Liu, W., Zhao, L., Sokolov, I. V., Whitman, K., Gombosi, T. I., Sachdeva, N., ... Tegnell, K. L. (2025, November). *Data based on the Study of Simulated Real-Time Testing of the Prototype Implementation of the SOFIE Model: The 2025 Space Weather Prediction Testbed Exercise*. Zenodo. doi: 10.5281/zenodo.17574017
- Löwe, J. L., Khaksarighiri, S., Wimmer-Schweingruber, R. F., Hassler, D. M., Ehresmann, B., Guo, J., ... others (2025). Nowcasting Solar Energetic Particle Events for Mars Missions. *Space Weather*, *23*(4), e2025SW004372. doi: 10.1029/2025SW004372
- Luhmann, J., Mays, M., Li, Y., Lee, C., Bain, H., Odstrcil, D., ... Petrie, G. (2018). Shock Connectivity and the Late Cycle 24 Solar Energetic Particle Events in July and September 2017. *Space Weather*, *16*(5), 557–568. doi: 10.1029/2018SW001860
- Manchester, W., Gombosi, T. I., Roussev, I., Ridley, A., De Zeeuw, D. L., Sokolov, I., ... Tóth, G. (2004). Modeling a Space Weather Event from the Sun to the Earth: CME Generation and Interplanetary Propagation. *Journal of Geophysical Research: Space Physics*, *109*(A2). doi: 10.1029/2003JA010150
- Manchester, W., Kilpua, E. K., Liu, Y. D., Lugaz, N., Riley, P., Török, T., & Vršnak, B. (2017). The Physical Processes of CME/ICME Evolution. *Space Science Reviews*, *212*, 1159–1219. doi: 10.1007/s11214-017-0394-0

- Mays, M., Taktakishvili, A., Pulkkinen, A., MacNeice, P., Rastätter, L., Odstrcil, D., ... others (2015). Ensemble Modeling of CMEs Using the WSA-ENLIL+Cone Model. *Solar Physics*, *290*, 1775–1814. doi: 10.1007/s11207-015-0692-1
- Menzel, W. P., & Purdom, J. F. (1994). Introducing GOES-I: The First of a New Generation of Geostationary Operational Environmental Satellites. *Bulletin of the American Meteorological Society*, *75*(5), 757–782. doi: 10.1175/1520-0477(1994)075<0757:IGITFO>2.0.CO;2
- Mertens, C. J., & Slaba, T. C. (2019). Characterization of Solar Energetic Particle Radiation Dose to Astronaut Crew on Deep-Space Exploration Missions. *Space Weather*, *17*(12), 1650–1658. doi: 10.1029/2019SW002363
- Minow, J. I., Mertens, C. J., Parker, L. N., Allen, J. R., Fry, D. J., Semones, E. J., ... others (2020). Space Weather Architecture Options to Support Human and Robotic Deep Space Exploration. *NASA Technical Paper 20205000837*. Retrieved from <https://ntrs.nasa.gov/citations/20205000837>
- Onsager, T., Grubb, R., Kunches, J., Matheson, L., Speich, D., Zwickl, R. W., & Sauer, H. (1996). Operational uses of the GOES energetic particle detectors. In *GOES-8 and Beyond* (Vol. 2812, pp. 281–290). Retrieved from <https://doi.org/10.1117/12.254075> doi: 10.1117/12.254075
- Papaioannou, A., Sandberg, I., Anastasiadis, A., Kouloumvakos, A., Georgoulis, M. K., Tziotziou, K., ... Hilgers, A. (2016). Solar flares, coronal mass ejections and solar energetic particle event characteristics. *Journal of Space Weather and Space Climate*, *6*, A42. doi: 10.1051/swsc/2016035
- Papaioannou, A., Strauss, R. D. T., Lario, D., Vainio, R., Wijsen, N., Afanasiev, A., ... Kouloumvakos, A. (2025). Predicting Solar Energetic Particles: Solar Storm Watch-Preparing for Space Odyssey. *Space Science Reviews*, *221*(6), 1–45. doi: 10.1007/s11214-025-01211-4
- Papaioannou, A., Vasalos, G., Whitman, K., Quinn, P., Anastasiadis, A., Mays, M. L., ... others (2025). Exploring the Validation Results of the Advanced Solar Particle Events Casting System (ASPECS). *Space Weather*, *23*(11), e2024SW004269. doi: 10.1029/2024SW004269
- Parker, E. N. (1965). The Passage of Energetic Charged Particles through Interplanetary Space. *Planetary and Space Science*, *13*(1), 9–49. doi: 10.1016/0032-0633(65)90131-5

- Posner, A., Hesse, M., & St. Cyr, O. (2014). The main pillar: Assessment of space weather observational asset performance supporting nowcasting, forecasting, and research to operations. *Space Weather*, *12*(4), 257–276. doi: 10.1002/2013SW001007
- Richardson, I. G., von Rosenvinge, T. T., & Cane, H. V. (2015). The Properties of Solar Energetic Particle Event-Associated Coronal Mass Ejections Reported in Different CME Catalogs. *Solar Physics*, *290*(6), 1741–1759. doi: 10.1007/s11207-015-0701-4
- Rodriguez, J., Krosschell, J., & Green, J. (2014). Intercalibration of GOES 8–15 solar proton detectors. *Space Weather*, *12*(1), 92–109. doi: 10.1002/2013SW000996
- Scherrer, P. H., Bogart, R. S., Bush, R., Hoeksema, J.-a., Kosovichev, A., Schou, J., ... others (1995). The solar oscillations investigation-Michelson Doppler imager. *Solar Physics*, *162*(1), 129–188. doi: 10.1007/BF00733429
- Shen, C., Wang, Y., Ye, P., & Wang, S. (2008). Enhancement of Solar Energetic Particles During a Shock–Magnetic Cloud Interacting Complex Structure. *Solar Physics*, *252*(2), 409–418. doi: 10.1007/s11207-008-9268-7
- Sokolov, I., Zhao, L., Liu, W., Biro, N., & Gombosi, T. (2025, October). *Daily Background Solar Wind Pipeline - Current Status and Future Plans*. Zenodo. doi: 10.5281/zenodo.17382521
- Sokolov, I. V., Roussev, I., Gombosi, T., Lee, M., Kóta, J., Forbes, T., ... Sakai, J. (2004). A New Field Line Advection Model for Solar Particle Acceleration. *The Astrophysical Journal*, *616*(2), L171. doi: 10.1086/426812
- Sokolov, I. V., van der Holst, B., Manchester, W., Ozturk, D. C. S., Sente, J., Takishvili, A., ... Gombosi, T. I. (2021). Threaded-field-line Model for the Low Solar Corona Powered by the Alfvén Wave Turbulence. *The Astrophysical Journal*, *908*(2), 172. doi: 10.3847/1538-4357/abc000
- Sokolov, I. V., van der Holst, B., Oran, R., Downs, C., Roussev, I. I., Jin, M., ... Gombosi, T. I. (2013). Magnetohydrodynamic Waves and Coronal Heating: Unifying Empirical and MHD Turbulence Models. *The Astrophysical Journal*, *764*(1), 23. doi: 10.1088/0004-637X/764/1/23
- Sokolov, I. V., Zhao, L., & Gombosi, T. I. (2022). Stream-aligned Magnetohydrodynamics for Solar Wind Simulations. *The Astrophysical Journal*, *926*(1), 102.

- doi: 10.3847/1538-4357/ac400f
- Stanzione, D., West, J., Evans, R. T., Minyard, T., Ghattas, O., & Panda, D. K. (2020). Frontera: The Evolution of Leadership Computing at the National Science Foundation. In *Practice and experience in advanced research computing 2020: Catch the wave* (p. 106–111). Association for Computing Machinery. doi: 10.1145/3311790.3396656
- Thernisien, A., Chua, D., Carter, M., Rich, N., Noya, M., Babich, T., . . . others (2025). The CCOR Compact Coronagraphs for the Geostationary Operational Environmental Satellite-19 (GOES-19) and the Space Weather Follow On (SWFO) Missions. *arXiv preprint arXiv:2508.13467*. doi: 10.48550/arXiv.2508.13467
- Tóth, G., Sokolov, I. V., Gombosi, T. I., Chesney, D. R., Clauer, C. R., de Zeeuw, D. L., . . . Kóta, J. (2005). Space Weather Modeling Framework: A New Tool for the Space Science Community. *Journal of Geophysical Research: Space Physics*, 110(A12). doi: 10.1029/2005JA011126
- Tóth, G., van der Holst, B., Sokolov, I. V., De Zeeuw, D. L., Gombosi, T. I., Fang, F., . . . Opher, M. (2012). Adaptive numerical algorithms in space weather modeling. *Journal of Computational Physics*, 231(3), 870–903. doi: 10.1016/j.jcp.2011.02.006
- van der Holst, B., Sokolov, I. V., Meng, X., Jin, M., Manchester, W., Tóth, G., & Gombosi, T. I. (2014). Alfvén wave solar model (AWSoM): coronal heating. *The Astrophysical Journal*, 782(2), 81. doi: 10.1088/0004-637X/782/2/81
- Whitman, K., Egeland, R., Allison, C., Quinn, P., & Stegeman, L. (2026). Validation of Solar Energetic Particle Forecasting Models for Space Radiation Operations with SPHINX and VIVID. *NASA Technical Paper 20260000463*. Retrieved from <https://ntrs.nasa.gov/citations/20260000463>
- Whitman, K., Egeland, R., Quinn, P., Stegeman, L., Allison, C., Dierckxsens, M., . . . Bain, H. (2024). A Multi-Year Effort to Forward the Validation of Solar Energetic Particle Prediction Models. In *Triennial Earth-Sun Summit*. Retrieved from <https://ntrs.nasa.gov/citations/20240004144>
- Whitman, K., Egeland, R., Richardson, I. G., Allison, C., Quinn, P., Barzilla, J., . . . others (2023). Review of Solar Energetic Particle Prediction Models. *Advances in Space Research*, 72(12), 5161–5242. doi: 10.1016/j.asr.2022.08.006

- Wraback, E., Hoffmann, A., Manchester, W., Sokolov, I., van der Holst, B., & Carpenter, D. (2024). Simulating Compressive Stream Interaction Regions during Parker Solar Probe's First Perihelion Using Stream-aligned Magnetohydrodynamics. *The Astrophysical Journal*, *962*(2), 182. doi: 10.3847/1538-4357/ad21fd
- Zank, G., Rice, W., & Wu, C. (2000). Particle acceleration and coronal mass ejection driven shocks: A theoretical model. *Journal of Geophysical Research: Space Physics*, *105*(A11), 25079–25095. doi: 10.1029/1999JA000455
- Zhao, L., Sokolov, I., Gombosi, T., Lario, D., Whitman, K., Huang, Z., . . . Liu, W. (2024). Solar Wind With Field Lines and Energetic Particles (SOFIE) Model: Application to Historical Solar Energetic Particle Events. *Space Weather*, *22*(9), e2023SW003729. doi: 10.1029/2023SW003729
- Zhong, Y., Wang, Y., & Qin, G. (2024). The Mean Free Path of 13–64 MeV Protons Derived from Statistical Results of Solar Energetic Particle Events. *The Astrophysical Journal*, *974*(2), 228. doi: 10.3847/1538-4357/ad70aa
- Zhuang, B., Lugaz, N., Gou, T., Ding, L., & Wang, Y. (2020). The Role of Successive and Interacting CMEs in the Acceleration and Release of Solar Energetic Particles: Multi-viewpoint Observations. *The Astrophysical Journal*, *901*(1), 45. doi: 10.3847/1538-4357/abaef9